Performance Analysis of Tracking Loops in Highly Dynamical Environments

Master Thesis

Institute for Navigation and Communication
Prof. Dr. sc. nat. Christoph Günther

Supervised by:
Dipl.-Ing. Kaspar Giger
MSc. Rachid El-Assir

by:
Nabil Ghanem

Munich, October 20, 2009

"To the two people who gave me all their support during the last 24 years of their lives, my beloved parents Wajdi and Nadia"

Acknowledgements

Abstract

In this work the effect of high receiver dynamics on several tracking techniques, used in Global Navigation Satellite Systems (GNSS) receivers, is studied. It is shown that code tracking experiences the least of this effect and need not be adapted. Moreover, traditional Phase Locked Loop carrier tracking is simulated under high dynamics. The conventional linearized simulation model was extended to mimic the exact signal correlation process under high acceleration. Intermediate frequency simulations were also carried for validation of the results. The new mathematical representation of the correlation process gives high inspiration for an accurate measurement model to be used in an Extended Kalman Filter (EKF) tracking system. Accordingly an enhanced EKF is developed and compared to various EKF carrier tracking system available in the literature. The proposed solution shows its ability to withstand the most severe dynamics situations amongst other EKF solutions with simpler measurement models. Furthermore, while other solutions do not benefit from the second order EKF implementation whose aim is to reduce the linearization error, the enhanced measurement form shows a further improvement in a second order Kalman filter scheme. EKF tracking was studied further with Numerically Controlled Oscillators (NCO) of higher order and it was shown that the frequency controlled NCO remains the most suitable solution. Additionally, the EKF tracking solution is compared to the PLL solution on a fair basis, where the noise bandwidth of the PLL was chosen to promote its best performance. The EKF shows a generally better performance for weak signals than that of PLL tracking. Precisely, in low dynamics situations with a carrier to noise ratio weaker than 24 dB-Hz the proposed EKF is better, while the PLL performance is better with higher carrier to noise ratios. Moreover, in high dynamics situations the margin where EKF tracking outperforms PLL tracking extends to higher values of carrier to noise ratio.

Contents

List of Figures

iv

List of Tables

Chapter 1

Introduction

Rapidly changing receiver dynamics are known to deteriorate the tracking performance of traditional Global Navigation Satellite Systems (GNSS) receivers. While current systems use PLL for tracking, they are suboptimal in compromising the effects of noise and dynamics simultaneously. The purpose of this study was initially to develop a PLL simulator to analyze the tracking performance of Phase Locked Loops (PLL) in high dynamics scenarios. In doing so, it was observed that an Extended Kalman Filter (EKF) may be a more optimal solution in high acceleration scenarios and performs well with higher order dynamics.

After the acquisition stage, the initial code phase and carrier frequency offset are estimated by the receiver. Nevertheless, these parameters are time changing and must be tracked. Several reasons stand behind this time varying aspect of the channel. First and most importantly is the receiver motion making the line of sight dynamics rapidly varying. In several case the receiver motion can result in sever consequences as is it sometimes hard to predict. Secondly is the satellite motion in addition to the changing atmospheric conditions leading to a varying doppler shift. However these later effects are smaller and more predictable.

Although both the carrier and the code experience the same effects, the code sequence, suffers from a much milder fashion. The effects on the code are reduced because the doppler shift is inversely proportional to the wave length. This makes the effects on the code, which has a much larger wavelength, much smaller than it is on the carrier .

In section 1.1 of this chapter a signal model including the dynamics is presented. In section 1.2 a performance measure is presented and it parameters are defined. Chapter 2 discusses the effect of high dynamics on the code tracking while in chapter 3 a simulation model for high dynamics is built in order to compare the loop performance in several noise and dynamics situation. The developed PLL simulation model gives a high inspiration for an actual carrier tracking solution using EKF. The EKF solution is discussed in chapter 4. Finally this work is
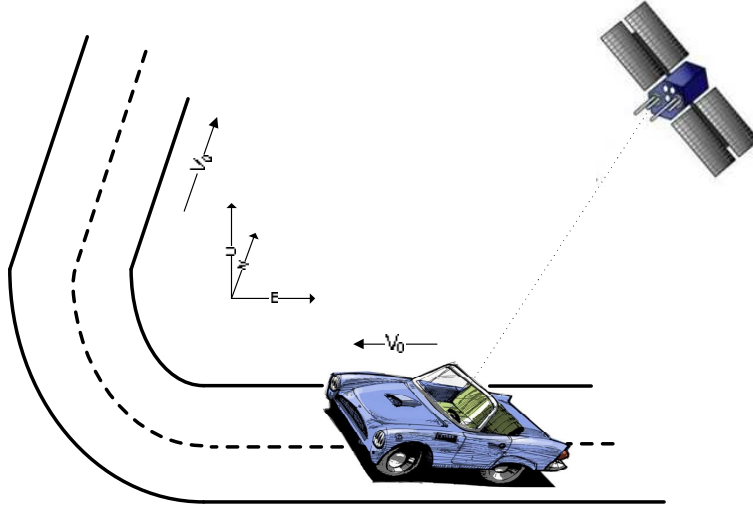
Figure 1.1: Typical scenario of high dynamics

concluded in chapter 5.

1.1   High Dynamics and signal model

Line of Sight (LOS) changes in the signal will be considered, reducing the focus of this work to a single channel of a stand alone receiver. This simplification is valid under the considerations and purpose of this study. In fact, dynamics taking place in the LOS direction are the most intense, hence making the LOS dynamics more interesting to look at. Indeed it is, because consider otherwise the case where the dynamics happen in the orthogonal direction to the LOS vector, then they will not be be seen by the receiver and have no effect on the tracking performance. However, a LOS dynamics model would not be sufficient when more sophisticated tracking techniques are to be considered. For instance, joint tracking would require the understanding of the whole geometry of the constellation instead of focusing on a single tracking channel. These multichannel tracking methods are left outside the scope of this work, hence giving the advantage of simplifying the signal model to a LOS model.

A Taylor series expansion for the carrier phase term around $t = 0$ is presented in what follows. For convenience, we first separate the contribution of the receiver dynamics from other effects. We then merge them together for desired simplicity in the model.

$$\Phi_{rcv}(t) = \frac{2\pi}{\lambda}(r_0 + v_0 t + \frac{a_0}{2}t^2 + \frac{j_0}{6}t^3 + ...) \tag{1.1}$$

$$\Phi_{sv}(t) = \phi_{0sv} + \omega_{D0} t + \frac{\dot{\omega}_{D0}}{2}t^2 + \frac{\ddot{\omega}_{D0}}{6}t^3 + ...) \tag{1.2}$$

$$S(t) = \cos(\omega_c t + \Phi_{rcv}(t) + \Phi_{sv}(t)) \tag{1.3}$$

Where equation (1.1) describes the receiver's dynamics and equation (1.2) describes dynamics counterpart due to satellite position and movements in addition to the atmospheric effects which are implicitly included in ω_{D0} and its derivatives. In both equations (1.1) and (1.2), the derivatives of the frequency equivalent terms are considered to additionally include the change of the frequency component due to the change in the direction of the LOS vector. For instance if the receiver's absolute velocity is constant but it is experiencing a change in its direction, such the case is in figure 1.1, then the rate of change of the LOS velocity would be considered as acceleration, jerk and higher order terms.

Nevertheless, as our aim of this work is to analyze the effect of high dynamics, the low dynamics coming from the SV, expressed in $\Phi_{sv}(t)$, can be neglected. The minor shortcoming in doing so is that any numerical mention of the LOS receiver dynamics is not accurate in the sense that the receiver motion is not the only contributor in the stated LOS value. This becomes important when generating a receiver data sheet for example where the maximum allowed dynamics are stated. If this is the case, worst case values of $\dot{\omega}_{D0}$ and $\dot{\omega}_{D0}$ should be subtracted. After profiling a high amount of simulated GPS signal, such a worst case value of $\dot{\omega}_{D0}$ is around $5 \sim 6Hz/s$. $\ddot{\omega}_{D0}$ is expected to be negligible as the satellite dynamics are slow. Moreover, this simplification can be further backed up by the fact the impact of receiver dynamics is much higher especially on acceleration and higher order term. For instance, a propeller driven aircraft performing a 10 seconds horizontal loop would experience a maximum doppler change rate of $400Hz/s$ equivalent to $a_0 = 12.5m/s^2$, that is well higher then the aforementioned figure of $5 \sim 6Hz/s$. Cars changing direction more rapidly experience also high equivalent a_0.

Having that said, we now merge $\Phi_{rcv}(t)$ and $\Phi_{sv}(t)$ as follows, reaching the

LOS dynamics model presented in equations (1.4) and (1.5).

$$\Phi(t) = \Phi_{rcv}(t) + \Phi_{sv}(t) = \phi_0 + \omega_0 t + \frac{\dot{\omega}_0}{2}t^2 + \frac{\ddot{\omega}_0}{6}t^3 + ... \tag{1.4}$$

$$\phi_0 = \frac{2\pi}{\lambda}r_0 + \phi_{0sv}$$

$$\omega_0 = \frac{2\pi}{\lambda}v_0 + \omega_{D0}$$

$$\dot{\omega}_0 = \frac{2\pi}{\lambda}a_0 + \dot{\omega}_{D0}$$

$$\ddot{\omega}_0 = \frac{2\pi}{\lambda}j_0 + \ddot{\omega}_{D0}$$

$$S(t) = \cos(\omega_c t + \Phi(t)) \tag{1.5}$$

Finally, for more convenience, it might happen that we mention in what follows of this document the terms acceleration and jerk. Hence, otherwise stated, these terms will be considered to include the channel dynamics as well.

1.2 Tracking Loops Performance

Tracking loops usually face two limiting factors. The first factor is the low Carrier to Noise ratio C/N_0 and the second is the disturbance created by high and changing dynamics conditions. Unfortunately, a solution that solves both problems simultaneously is impossible as there is always a need for some kind of compromise depending on the situation. For instance, in a traditional Phase Locked Loop (PLL), the loop bandwidth B_n is a parameter that can be used to such adaptation in situations where we have knowledge about the noise. Precisely, in noisy scenarios a tight bandwidth is needed, however this comes at a price of a limited resistance to dynamics stress. Oppositely, a large bandwidth will help the loop remaining in lock state with higher dynamics stress conditions, but this will of course require a low enough noise level.

The performance of tracking loops is then assessed based on these two factors. The immunity to noise is measured by the phase error jitter. Whereas the immunity to dynamics stress is determined by the order and intensity of the dynamics. The higher the loop order is, the more orders of dynamics become transparent to the loop. Namely, velocity is transparent to a second order loop whereas acceleration is transparent to a third order loop. Furthermore, for a third order loop, the amount of jerk stress allowed could serve as a measuring factor for the immunity to dynamics stress. It is important here to distinguish between the effect of noise, which increases the jitter (i.e. standard deviation of the error) in the phase estimate, and the effect of high dynamics (e.g. jerk stress), which would lead to a
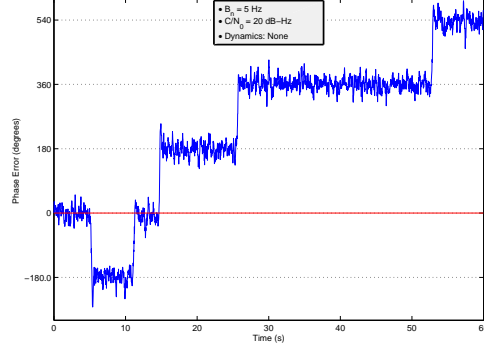
Figure 1.2: An example of the cycle slip phenomenon

bias in the estimate. At the end of the loop performance analysis, the jitter and the bias should both add up to a phase error value less than a specific threshold, discussed further in the next paragraph.

For a non-modulated sinusoidal signal, the loop is said to maintain the lock whenever the replica generated by the Numerically Controller Oscillator (NCO) has a phase that is close to the phase of the incoming signal by significantly less than one cycle. Here comes the notion of the 3-sigma threshold. This threshold uses a probabilistic approach and basically suggests that the 3-sigma jitter should not increase one fourth of the PLL pull in range as follows

$$3 \cdot \sigma_{PLL} = 3 \cdot \sigma_i + \theta_e \leq 90° \tag{1.6}$$

where:

σ_i = 1-sigma phase jitter from all sources except the dynamics stress. This means in our case the thermal noise as the jitter due to oscillator is also out of the scope of our study. θ_e = dynamics stress error in the PLL

In some cases, especially when a noisy signal experiences an extra burst of noise for a very short period of time, the estimated phase error increases up to more than one cycle. However the loop regains the lock state directly afterwards. This is known as a cycle slip. Algorithms that detect cycle slips have been subject to many studies, but they remain outside the scope of this discussion. When cycle slips become more frequent, it is highly probable that the loop will lose the lock completely. An example of a case with frequent cycle slips is shown in figure 1.2

Furthermore, for a sinusoidal signal modulated with binary data, a flip in the sign of the incoming waveform should be expected at anytime. To accomplish an phase error estimate which regardless of the sign, the loop is usually equipped with an atan(·) discriminator. This later has a period of half a cycle, making the

6

requirement on the the 3-sigma threshold to be

$$3 \cdot \sigma_{PLL} = 3 \cdot \sigma_i + \theta_e \leq 45° \quad (1.7)$$

In fact, as the pull-in range of the atan($\cdot$) discriminator is half a cycle, the same slips effect described before is now called half-cycle slips. In fact, this is what figure 1.2 shows.

Chapter 2

Code Tracking Loop

The code tracking loop, also known as Delay Locked Loop (DLL), is one counterpart of the signal tracking in a GNSS receiver. Hence, it constitutes along with the carrier tracking loop the most critical component, that is the signal tracking module. Although the two loops are highly coupled, the DLL usually receives Doppler aiding from the carrier tracking. Using this information the DLL adjust its replica code rate accordingly to compensate for this effect. In this chapter we study the effect of acceleration and jerk on the isolated DLL for a single accumulate and dump period where specifically the correlation procedure is investigated. The result we will come to in this chapter shows that the effects are negligible. The conclusions can be made without the burden of going into further analysis of the closed loop.

The results derived here are not surprising. In fact the code rate is much lower than the carrier, the impacts of high dynamics are expected to be milder on code tracking than it is on carrier tracking. The latter is to be studied later.

2.1 The Effect of High Dynamics on the Autocorrelation

The code generated at the SV can be written as a function of time as follows:

$$\mathcal{C}_{sv}(t) = \sum_{k=1}^{N} c_k \text{Rect}\left(\frac{t - kT_c}{T_c}\right) \tag{2.1}$$

Where $\text{Rect}(\cdot)$ is the rectangular[1] function

---

[1]$\text{Rect}(x) = \begin{cases} 0 & \text{if } x < 0 \ \text{ or } \ x \geq 1 \\ 1 & \text{if } 0 \leq x < 1 \end{cases}$

With c_k being the value of the kth chip (± 1), T_c being the chip duration and N the code length in chips. The code is seen at the receiver at time t with is delayed by $d(t) = x_0 + v_0 t + \frac{a_0}{2}t^2 + \frac{j_0}{6}t^3$

With $d(t)$ being the line of sight dynamics including an initial distance x_0, velocity v_0, acceleration a_0 and jerk j_0. Hence the code seen at the receiver can be written as:

$$\mathcal{C}_r(t) = \mathcal{C}_{sv}\left(t - \frac{d(t)}{c}\right) = \sum_{k=1}^{N} c_k \text{Rect}\left(\frac{t(1 - \frac{v_0}{c} - \frac{a_0}{2c}t - \frac{j_0}{6c}t^2) - kT_c - \frac{x_0}{c}}{T_c}\right) \quad (2.2)$$

Note that x_0 is nothing but the pseudorange shift resolved by synchronizing the code and its replica so it can be neglected. Moreover, $\frac{v_0}{c}$ is nothing but the doppler shift which is perfectly known from the tracking loop. In fact, in the carrier aided code loop, the code replica is sampled according to this value which means that it can also be neglected. Therefore, 2.2 becomes:

$$\begin{aligned}
\mathcal{C}_r(t) &= \sum_{k=1}^{N} c_k \text{Rect}\left(\frac{t(1 - \frac{a_0}{2c}t - \frac{j_0}{6c}t^2) - kT_c}{T_c}\right) \\
&= \sum_{k=1}^{N} c_k \text{Rect}\left(\frac{t - \frac{kT_c}{(1 - \frac{a_0}{2c}t - \frac{j_0}{6c}t^2)}}{T_c \frac{1}{(1 - \frac{a_0}{2c}t - \frac{j_0}{6c}t^2)}}\right)
\end{aligned} \quad (2.3)$$

Using the approximation

$$\frac{1}{1 - x} \approx 1 + x \qquad for \qquad x \ll 1 \qquad with \qquad x = \frac{a_0}{2c}t + \frac{j_0}{6c}t^2 \quad (2.4)$$

we get a chip length seen at the receiver of

$$T_c' = \frac{T_c}{1 - \frac{a_0}{2c}t - \frac{j_0}{6c}t^2} \approx T_c\left(1 + \frac{a_0}{2c}t + \frac{j_0}{6c}t^2\right) \quad (2.5)$$

Assuming the tracking loop is tracking the dynamics perfectly then this value will accumulate only for one coherent integration duration. Thus, the maximum chip length will be $T_c\left(1 + \frac{a_0}{2c}T + \frac{j_0}{6c}T^2\right)$. Where T is the coherent integration duration.

For instance, for a 1023 chips long C/A code, choosing a typical the integration time of $T = 20$ ms with acceleration a_0 and jerk j_0 leads to a maximum increase (last chip) in the chip duration by $3.33 \cdot a_0 \cdot 10^{-11} + 2.22 \cdot j_0 \cdot 10^{-13}$ chips. Furthermore, the total shift of the code measured at the last chip will be ρ and is given as

$$\begin{aligned}
\rho &= \frac{a_0}{2c}T_c\frac{(N+1)N}{2} + \frac{j_0}{6c}T_c^2\frac{N(N+1)(2N+1)}{6} && (2.6) \\
&= a_0 \times 3.41 \ 10^{-7} + j_0 \times 1.5505 \times 10^{-3} \text{ chips} && (2.7) \\
&= a_0 \times 10^{-4} + j_0 \times 0.455 \text{ m}
\end{aligned}$$
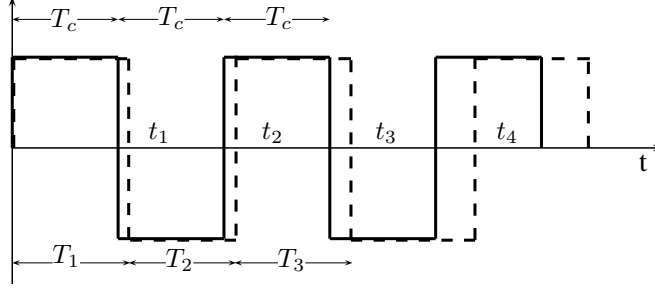
Figure 2.1: Received code with LOS acceleration (dashed) and code replica (solid)

Looking for a lower bound of the correlation output, lets conservatively assume low autocorrelation properties of the code, meaning that the code is an alternation of $+1$ and -1. This choice helps in the simplicity of the derivation and is enough for a tight bound as we shall see next.

Consider the received code and the locally generated replica, as shown in figure 4, to be synchronized at the start point of the integration duration. Let us also consider the quantity C_k to be the contribution to the correlation coming only from the kth chips. Relying on the figure we can write what follows:

$$C_1 = t_1 - (t_1 - T_c) = T_c$$
$$C_2 = t_2 - t_1 - (t_2 - 2T_c) = 2T_c - t_1$$
$$C_3 = t_3 - t_2 - (t_3 - 3T_c) = 3T_c - t_2$$

$$C_k = kT_c - t_{k-1} = kT_c - \sum_{l=1}^{k-1} T_l$$

$$R'(0) \geq \sum_{k=1}^{N} C_k = \sum_{k=1}^{N} \left(kT_c - \sum_{l=1}^{k-1} T_l \right) + \epsilon$$

Where $R'(0)$ is the correlation value with acceleration considering a zero initial time shift. $\epsilon \ll T_c$ is a small quantity rising from the fact that the integration takes place till the end of the local replica of the code and not the received one. Hence, it can be dropped as it doesn't help much tightening the approximation.

Next, using 2.5 with $t = t_k = \sum_{l=1}^{k-1} T_l$ with $T_l = T_c\big(1 + \frac{a_0}{2c} lT_c + \frac{j_0}{6c}(lT_c)^2\big)$ we calculate the ratio of the correlation $R'(0)$ with acceleration to the correlation $R(0)$ without acceleration as follows.

10

$$\frac{R'(0)}{R(0)} = \frac{R'(0)}{NT_c}$$

$$\geq \frac{1}{N}\sum_{k=1}^{N} k - \frac{1}{N}\sum_{k=1}^{N}\sum_{l=1}^{k-1}\left(1 + \frac{a_0}{2c}T_c l + \frac{j_0}{6c}T_c^2 l^2\right)$$

$$= \frac{1}{N}\sum_{k=1}^{N} k - \frac{1}{N}\sum_{k=1}^{N}\left[k - 1 + \frac{a_0}{2c}T_c\frac{(k-1)k}{2} + \frac{j_0}{6c}T_c^2\frac{(k-1)k(2k-1)}{6}\right]$$

$$= 1 - \frac{a_0}{4c}T_c\frac{1}{N}\sum_{k=1}^{N}(k^2 - k) - \frac{j_0}{36c}T_c^2\sum_{k=1}^{N}(2k^3 - 3k^2 + k)$$

$$= 1 - \frac{a_0}{4c}T_c\left[\frac{(N+1)(2N+1)}{6} - \frac{N+1}{2}\right]$$

$$\quad - \frac{j_0}{36c}T_c^2\left[\frac{N+1}{2} - \frac{(N+1)(2N+1)}{2} + \frac{N(N+1)^2}{2}\right]$$

$$= 1 - \frac{a_0}{12c}T_c(N+1)(N-1) - \frac{j_0}{72c}T_c^2(N+1)(N-1)N$$

$$= 1 - \frac{a_0}{12c}T_c(N^2 - 1) - \frac{j_0}{72c}T_c^2(N^2 - 1)N \tag{2.8}$$

Plugging in $N = 20 \times 1023$ which is equivalent to the maximal integration time of 20 ms with initial acceleration $a0 = 1000$ m/s^2 and jerk $j0 = 1000$ m/s^3 representing ultra hight dynamics we get:

$$\frac{R'(0)}{R(0)} \geq 0.999886 \tag{2.9}$$

Nevertheless, the degradation values are expected to be even less due the good autocorrelation properties of the C/A code. In the next we investigate this effect and we look further in the errors generated by the early late discriminator due to dynamics.

2.2 The effect of Integration Duration

Simulating the actual correlation process looks impractical. Therefore we extended the approximation above using MATLAB® to account for the pseudo-randomness of C/A codes. In this section we show these results along with the relationship to T the accumulate and dump duration.
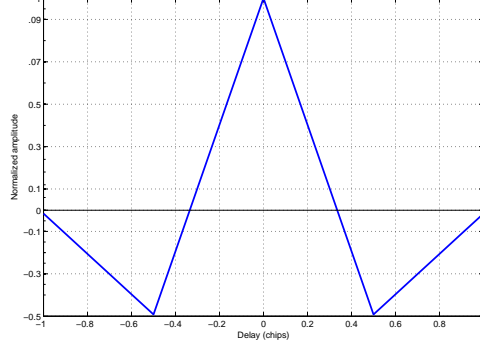
Figure 2.2: Autocorrelation Function of BOC(1,1) pilot C/A code for GIOVE-A
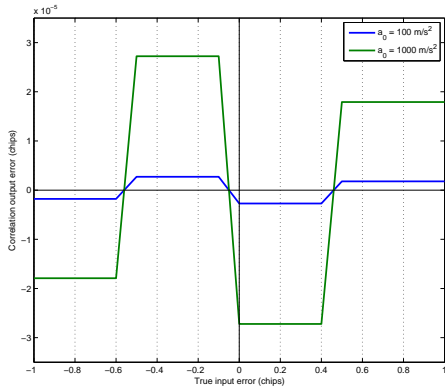
Figure 2.3: Correlation Error for two different acceleration values ($T = 8ms$)
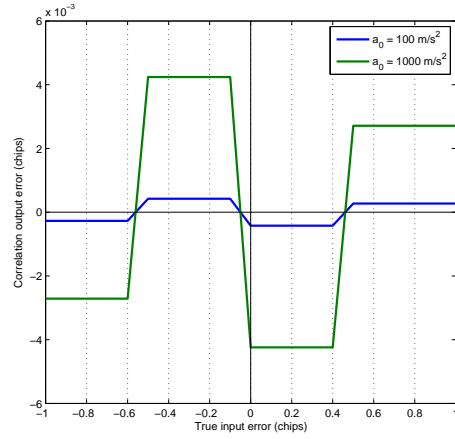
Figure 2.4: Correlation Error for two different acceleration values ($T = 100ms$)

Figure 2.2 show the autocorrelation for the BOC(1,1) C/A pilot code of the GIOVE-A satellite. Because the difference in the autocorrelation for several acceleration values cannot be graphically emphasized in figure 2.2, we show in figures 2.3 and 2.4 the error between autocorrelation plots for two different high acceleration values and two different accumulate and dump durations the the autocorrelation plot corresponding to zero acceleration. Additionally, an important aspect to observe is the constant error over the whole linear region, which is our region of interest. This leads us to measure the absolute tracking error.

Figures 2.8 and 2.9 summarize the code tracking error for the GIOVE-A and GPS-PRN-1 SVs. This error is evaluated for a range of accelerations and integration duration T. The first, observation is that the error increases linearly with
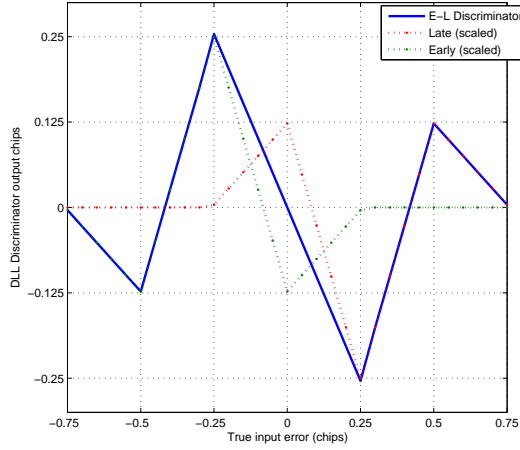
Figure 2.5: DLL discriminator of BOC(1,1) C/A pilot code for GIOVE-A
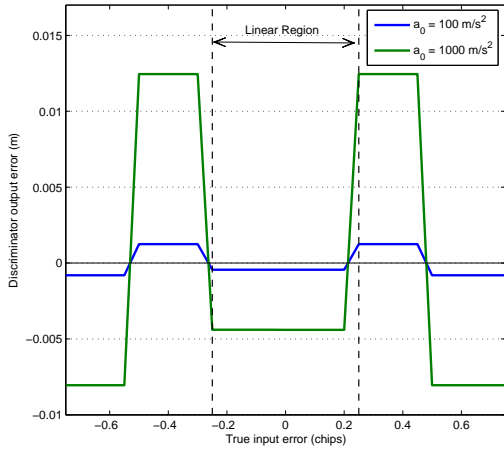
Figure 2.6: Discriminator error in meters for two different acceleration values ($T = 8ms$)
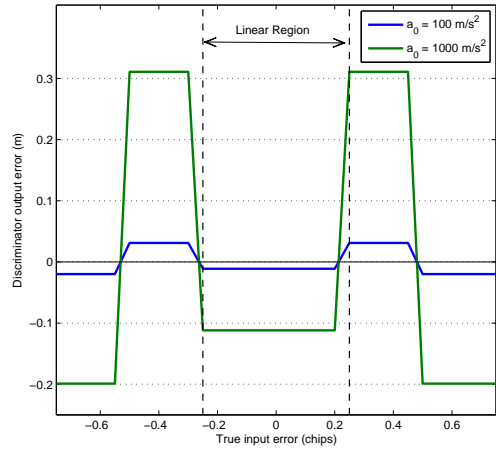
Figure 2.7: Discriminator error in meters for two different acceleration values ($T = 100ms$)

acceleration. However for the same acceleration the degradation with increased accumulate and dump period is more dramatic. This result could help opening some eyes on the limitations of long integration durations for the forthcoming Galileo pilot signals where the code tracking error could reach 3.5 cm in cases of very high acceleration.

Finally, even in the extreme cases considered, the degradation can still be ne-
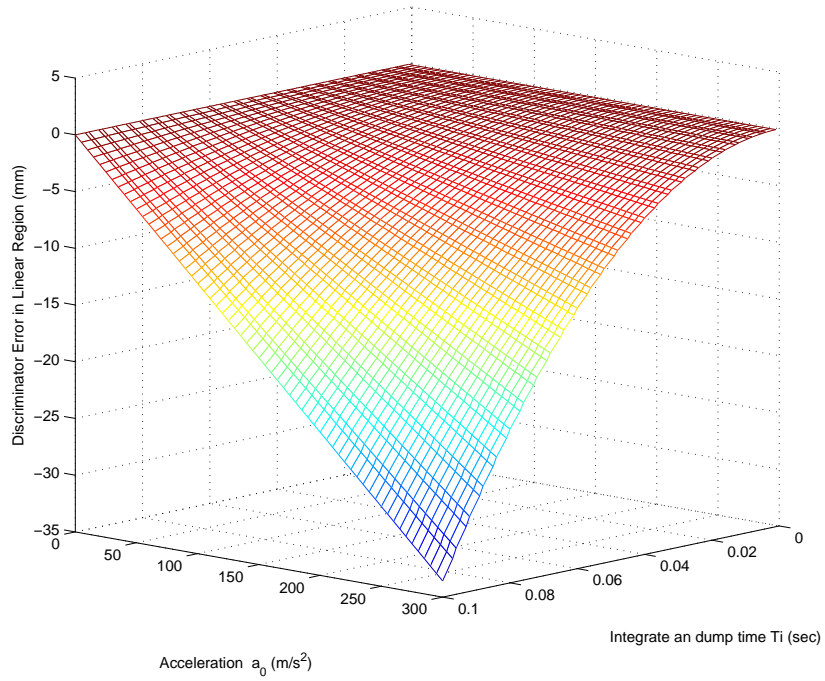
Figure 2.8: GIOVE-A pilot BOC(1,1): Discriminator Error in mm function of a_0 and T
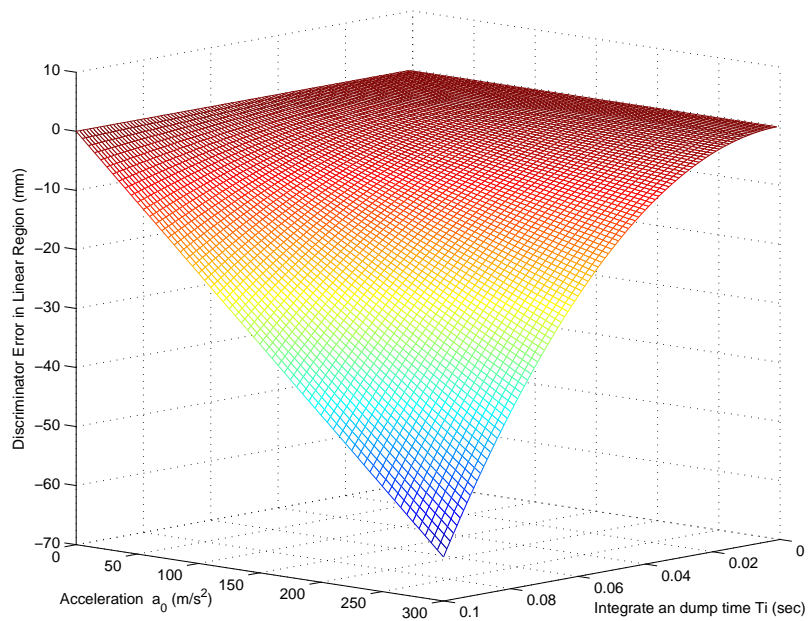
Figure 2.9: GPS: PRN-1: Discriminator Error in mm function of a_0 and T

14

glected. A loss of lock, for instance, would require an error to be a considerable fraction of a chip. The results here show this is improbable to happen even with extreme cases of dynamics. Therefore a conclusion can be made from this discussion that dynamics stress is transparent to carrier aided code loops. Therefore, the rest of this work focuses only on carrier tracking.

Chapter 3

Digital Phase Locked Loop

3.1   Overview

Analogue PLLs have proven to have a robust performance in several applications ranging from frequency and phase tracking to FM demodulation. After the evolution of CMOS technology and embedded systems, even the most time critical operation can be done digitally. Because of its robustness, digitizing the analogue PLL seemed to be the most agreeable approach targeting the tracking problem.

In fact some components do not witness any change in behavior when transforming the loop from analog to digital. Namely, discriminator hold the same characteristics except for minor quantization errors. The behavior of the loop filter is as well not expected to change from analogue to digital. However, both the NCO, used to be denoted as VCO, and the low pass filter do change the behavior. The accumulate and dump period , equivalently denoted as signal correlation duration, restrict the system to a given period T. T can be thought of as the sampling frequency at which the continuous PLL model is sampled, and a correct choice of this duration is critical for the stability of the loop, and generally of any transformation from a continuous to a discrete system. It is important however to distinguish here between T and T_s, the sampling period of the incoming signal. T is a design parameter that also determines how long should we correlate the incoming signal with the locally generated replica. Thus a very short T, although good for the responsiveness and immunity of the loop against dynamics stress, should take into consideration the noise factor. This is simply because the higher the correlation duration the better is the noise reduction. In other words, given a random variable, the additive noise in this case, if more instances are averaged then this average will be closer to the mean.

On the other side, the signal replica generated by the NCO has to have a constant frequency during one T duration, as the NCO input is updated once every
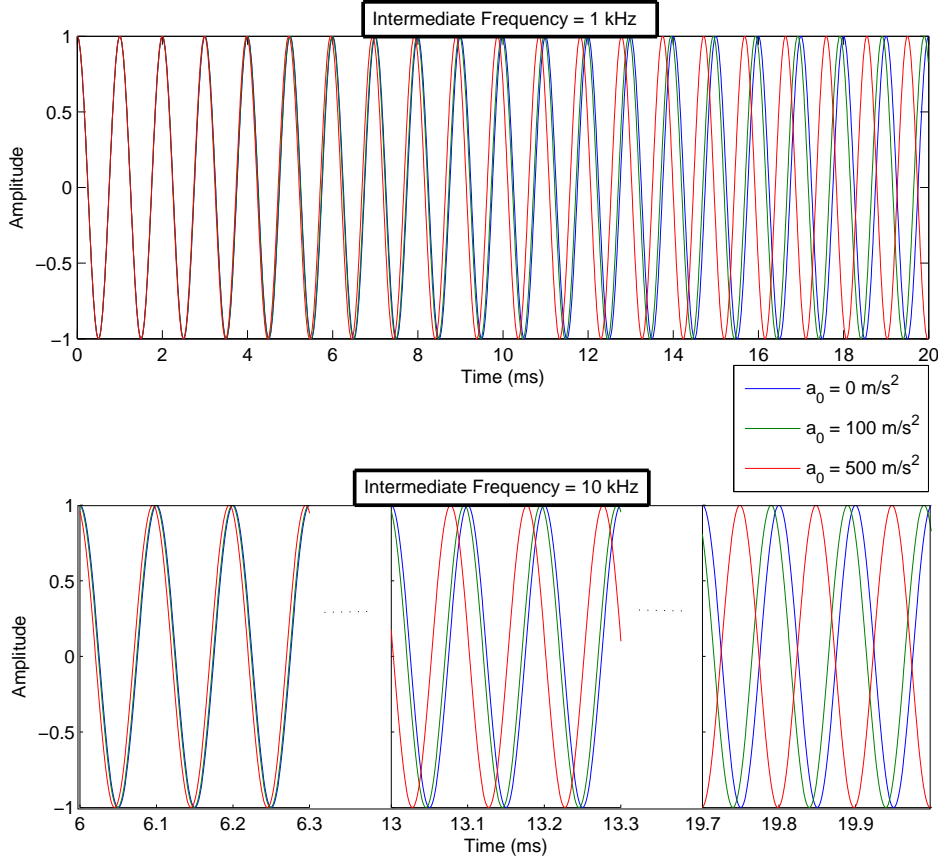
Figure 3.1: The effect of acceleration on the sinusoidal signal

T. Therefore, in contrast to the analogue PLL whose NCO frequency was continuously changed to adapt as best a possible to the incoming signal in hand, a digital PLL does not match the higher order component of the signal in its replica. To clarify the previous point, with an NCO that takes as input the frequency increments, the Doppler change rate, equivalently acceleration, and higher order terms will not be accurately modeled in the replica, however that does not necessarily mean that they are not accounted for by the lower order component of the NCO. Similarly , an NCO that takes the frequency change rate as input will act similarly with respect to jerk and higher order dynamics.

3.2   Linearized Loop Model

The linearized loop model, for both analogue and digital PLLs is a very handy tool for predicting the behavior of the PLL under certain conditions. The transfer
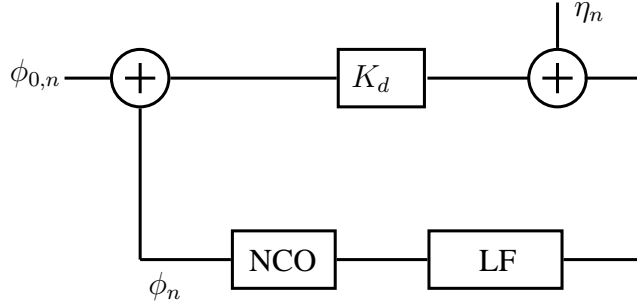
Figure 3.2: Linearized Loop Model

function of the first is expressed in the s-domain whereas in the z-domain for the latter. The main catch in the model is that it transforms the loop from the signal domain into the phase domain dropping out the actual signal-replica correlation process and the burden of its element by element multiplication. In addition to its usefulness in understanding analytically the loop behavior, it is also useful to build loop simulations that can run quickly with a high computational efficiency. Figure 3.2 shows the linearized loop model where the discriminator, loop filer and NCO are denoted by K_d, $F(z)$ and $N(z)$ respectively. In this model the discriminator is only a gain factor K_d. In fact linearization of the discriminator is the crucial step in the linearized model because most types of discriminator include trigonometric fuction such the atan($\cdot$) of the Costas loop. This linearization is valid and can be traced back to a $\sin(\delta\phi)$ discriminator model which may be approximated by $\sin(\Delta\phi) \approx \Delta\phi$.

Figure 3.3 represents the linearized model augmented for the purpose of simulating a Loop with an atan($\cdot$) discriminator, more precisely the Costas Loop. $G_I(\cdot)$ and $G_Q(\cdot)$ are the core component of the model, they simulate the accumulate and dump period providing I_n and Q_n as a function of the phase difference between the phase of the signal and the phase of the replica. In other terms they are transforms of the correlation from the signal domain to the phase domain. Furthermore, as we shall see in the derivation of $G_I(\cdot)$ and $G_Q(\cdot)$ will also depend on the frequency of the replica generated by the NCO as this gives better approximation. The inputs $\omega_{0,i}$ and $\alpha_{0,i}$ are external inputs which are thought of as a constants, whereas $\phi_{0,i}$ could be either a constant to simulate non changing dynamics or can be varied according to the simulation requirements. A useful simulation is to vary it according to phase profile modeling an acceleration random walk. We will tackle this point later in section 3.4. The input $\alpha_{0,i}$, is however disregarded in section 3.2.1.

In section 3.2.1 we show the traditional simulation model widely used in the domain of satellite tracking. Following, in section 3.2.2, we show a variation of this model where we introduce the effect of acceleration in the signal-replica correlation

18
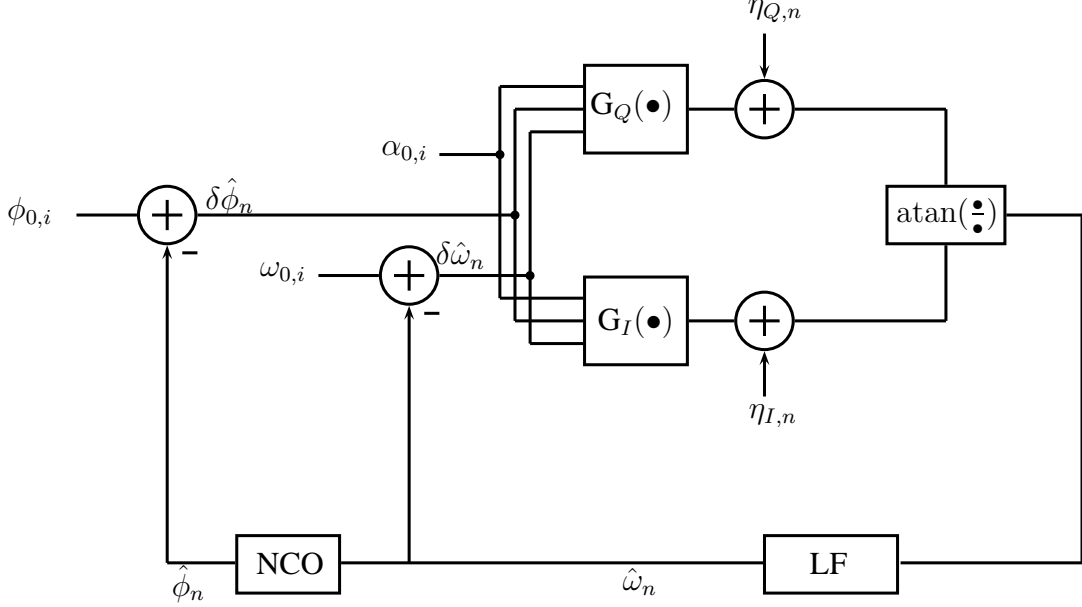
Figure 3.3: Costas Loop in Phase Domain

process.

3.2.1 Simulation Model without Acceleration

This simulation models the linear PLL for constant frequency and phase offsets ω_0 and ϕ_0 respectively. Equivalently this model applies only if the line of sight acceleration is zero. Following these considerations, the signal model $y(t)$ will be:

$$y(t) = \cos(\omega_c t + \omega_{0,n} t + \phi_{0,n}) \tag{3.1}$$

The locally generated replicas are:

$$y_{I,n}(t) = \cos(\omega_c t + \hat{\omega}_n t + \tilde{\phi}_n) \tag{3.2}$$

$$y_{Q,n}(t) = -\sin(\omega_c t + \hat{\omega}_n t + \tilde{\phi}_n) \tag{3.3}$$

Where $\tilde{\phi}_0$ is some starting phase that guarantees that the phase of the NCO is always continuous. Writing down the correlation equations we get the following

19

forms for I_n and Q_n:

$$
\begin{aligned}
I_n &= \frac{1}{T} \int_{(n-1)T}^{nT} y(t) y_{I,n}(t)\, dt \\
&= \frac{1}{T} \int_{(n-1)T}^{nT} \cos(\omega_c t + \omega_{0,n} t + \phi_{0,n}) \cos(\omega_c t + \hat{\omega}_n t + \tilde{\phi}_n)\, dt \\
&= \frac{1}{2T} \int_{(n-1)T}^{nT} \cos\left((\omega_{0,n} - \hat{\omega}_n)\, t + \phi_{0,n} - \tilde{\phi}_n\right) dt + \text{double freq term} \\
&= \frac{-1}{2T(\omega_{0,n} - \hat{\omega}_n)} \left[\sin\left((\omega_{0,n} - \hat{\omega}_n)(n-1)T + \phi_{0,n} - \tilde{\phi}_n\right) - \sin\left((\omega_{0,n} - \hat{\omega}_n)nT + \phi_{0,n} - \tilde{\phi}_n\right) \right] \\
&= -\frac{\sin\left(-\frac{T}{2}(\omega_{0,n} - \hat{\omega}_n)\right)}{T(\omega_{0,n} - \hat{\omega}_n)} \cos\left((\omega_{0,n} - \hat{\omega}_n)(n-1)T + (\omega_{0,n} - \hat{\omega}_n)\frac{T}{2} + \phi_{0,n} - \tilde{\phi}_n\right) \\
&= \frac{1}{2} \cdot \operatorname{sinc}^1\left(\frac{T}{2}(\omega_{0,n} - \hat{\omega}_n)\right) \times \cos\left((\omega_{0,n} - \hat{\omega}_n)(n-1)T + (\omega_{0,n} - \hat{\omega}_n)\frac{T}{2} + \phi_{0,n} - \tilde{\phi}_n\right)
\end{aligned}
$$
(3.4)

$$
\begin{aligned}
Q_n &= \frac{1}{T} \int_{(n-1)T}^{nT} y(t) y_{Q,n}(t)\, dt \\
&= \frac{1}{T} \int_{(n-1)T}^{nT} \cos(\omega_c t + \omega_{0,n} t + \phi_{0,n}) \times -\sin(\omega_c t + \hat{\omega}_n t + \tilde{\phi}_n)\, dt \\
&= \frac{1}{2T} \int_{(n-1)T}^{nT} \sin\left((\omega_{0,n} - \hat{\omega}_n)\, t + \phi_{0,n} - \tilde{\phi}_n\right) dt + \text{double freq term} \\
&= \frac{1}{2T(\omega_{0,n} - \hat{\omega}_n)} \left[\cos\left((\omega_{0,n} - \hat{\omega}_n)(n-1)T + \phi_{0,n} - \tilde{\phi}_n\right) - \cos\left((\omega_{0,n} - \hat{\omega}_n)nT + \phi_{0,n} - \tilde{\phi}_n\right) \right] \\
&= -\frac{\sin\left(-\frac{T}{2}(\omega_{0,n} - \hat{\omega}_n)\right)}{T(\omega_{0,n} - \hat{\omega}_n)} \sin\left((\omega_{0,n} - \hat{\omega}_n)(n-1)T + (\omega_{0,n} - \hat{\omega}_n)\frac{T}{2} + \phi_{0,n} - \tilde{\phi}_n\right) \\
&= \frac{1}{2} \cdot \operatorname{sinc}\left(\frac{T}{2}(\omega_{0,n} - \hat{\omega}_n)\right) \times \sin\left((\omega_{0,n} - \hat{\omega}_n)(n-1)T + (\omega_{0,n} - \hat{\omega}_n)\frac{T}{2} + \phi_{0,n} - \tilde{\phi}_n\right)
\end{aligned}
$$
(3.5)

Now we proceed to find $\tilde{\phi}_n$. A frequency jump will guarantee a continuous phase if the resulting phase at the end of one integration period to be equal to the phase at the beginning of the next one. Thus the following condition must be satisfied:

$$
(\omega_{0,n} - \hat{\omega}_n)(n-1)T + \tilde{\phi}_n = (\omega_{0,n-1} - \hat{\omega}_{n-1})(n-1)T + \tilde{\phi}_{n-1}
\tag{3.6}
$$

---

[1] $\operatorname{sinc}(x) = \frac{\sin(x)}{x}$

$$\tilde{\phi}_n = \left(\left(\omega_{0,n-1} - \hat{\omega}_{n-1} \right) - \left(\omega_{0,n} - \hat{\omega}_n \right) \right) (n-1)T + \tilde{\phi}_{n-1}$$

$$= \left(\left(\omega_{0,n-1} - \hat{\omega}_{n-1} \right) - \left(\omega_{0,n} - \hat{\omega}_n \right) \right) (n-1)T$$
$$\quad + \left(\left(\omega_{0,n-2} - \hat{\omega}_{n-2} \right) - \left(\omega_{0,n-1} - \hat{\omega}_{n-1} \right) \right) (n-2)T + \tilde{\phi}_{n-2}$$

$$= - \left(\omega_{0,n} - \hat{\omega}_n \right) (n-1)T + \left(\omega_{0,n-1} - \hat{\omega}_{n-1} \right) T + \left(\omega_{0,n-2} - \hat{\omega}_{n-2} \right) (n-2)T + \tilde{\phi}_{n-2}$$

$$\vdots$$

$$= - \left(\omega_{0,n} - \hat{\omega}_n \right) (n-1)T + \sum_{k=1}^{n-1} \left(\omega_{0,k} - \hat{\omega}_k \right) T$$

$$= - \left(\omega_{0,n} - \hat{\omega}_n \right) (n-1)T + \hat{\phi}_n \tag{3.7}$$

Where $\hat{\phi}_n = \sum_{k=1}^{n-1} \left(\omega_{0,k} - \hat{\omega}_k \right) T$ is the starting phase of the replica in the nth interval, given that the starting NCO phase is zero.

With

$$\delta\hat{\phi}_n = \phi_{0,n} - \hat{\phi}_n \tag{3.8}$$

$$\delta\hat{\omega}_n = \omega_{0,n} - \hat{\omega}_n \tag{3.9}$$

and replacing the result of 3.7 in equations 3.4 and 3.5 we get:

$$I_n = G_I^{(1)}(\delta\hat{\phi}_n, \delta\hat{\omega}_n) = \operatorname{sinc}\left(\delta\hat{\omega}_n T \right) \times \cos\left(\delta\hat{\omega}_n \frac{T}{2} + \delta\hat{\phi}_n \right) \tag{3.10}$$

$$Q_n = G_Q^{(1)}(\delta\phi_n, \delta\hat{\omega}_n) = \operatorname{sinc}\left(\delta\hat{\omega}_n T \right) \times \sin\left(\delta\hat{\omega}_n \frac{T}{2} + \delta\hat{\phi}_n \right) \tag{3.11}$$

This will lead to a discriminator output

$$D_n = \operatorname{atan}\left(\frac{Qn + \eta_{Q,n}}{In + \eta_{I,n}} \right) = \operatorname{atan}\left(\frac{\operatorname{sinc}\left(\delta\hat{\omega}_n T \right) \times \sin\left(\delta\hat{\omega}_n \frac{T}{2} + \delta\hat{\phi}_n \right) + \eta_{Q,n}}{\operatorname{sinc}\left(\delta\hat{\omega}_n T \right) \times \cos\left(\delta\hat{\omega}_n \frac{T}{2} + \delta\hat{\phi}_n \right) + \eta_{I,n}} \right) \tag{3.12}$$

When the noise terms η_I and η_Q vanish the $\operatorname{atan}(\cdot)$ discriminator output becomes:

$$D_n = \delta\hat{\omega}_n \frac{T}{2} + \delta\hat{\phi}_n \tag{3.13}$$

Equation (3.13) shows us that the $\operatorname{atan}(\cdot)$ discriminator estimates the phase error by averaging the phase error over the whole integration interval n.

Because of its simplicity to be implemented and its reduced complexity, this model is very useful when we aim at simulating the effect of noise on the PLL.

However, neglecting the Doppler change rate term in the actual signal implies that acceleration cannot be directly simulated. In other terms, the signal dynamics are represented only by the initial phase and frequency offsets. Therefore, in a lock state the only factor that can make the PLL loose lock or cause cycle slips is noise.

Nevertheless, one can use the aforementioned approach to simulate a constant acceleration and/or a constant jerk dynamics, which is adding the accumulated phase change caused by the acceleration (and/or jerk dynamics) in a single interval to the external phase input $\phi_{0,n}$. Moreover while $\omega_{0,n}$ is kept constant to ω_d the initial Doppler shift. Nevertheless, in order to generate a plausible stream of $\phi_{i,n}$ values, one would need to model the system according to some linear model including disturbances. This is provided later in section 4.2. The drawback of this approach is in simulating very high dynamics. A high and constant acceleration for example would create a step-wise changing doppler in steps every T. This will bias the simulation result as it will be hard to distinguish whether a loss of lock is due to noise or the transient effect due these doppler steps. To conclude, we will only retrain to use this model for cases with no acceleration or higher dynamics.

3.2.2   Simulation Model with Acceleration

In nowadays digital tracking loops, the NCO generates a constant a frequency signal during one integration period. Thus the carrier replica cannot perfectly match the acceleration signal. Hence, in order to study the effect of acceleration on jitter, we need to simulate the exact behavior of the integrate and dump step. And therefore, in contrast to the previous model, we add here a constant acceleration term to the signal phase. The derivation carried in the previous section will now look as follows:

$$y(t) = \cos(\alpha_{0,n}t^2 + \omega_c t + \omega_{0,n}t + \phi_{0,n}) \qquad \text{with } \alpha_{0,n} = \frac{2\pi}{\lambda}\frac{a_0}{2} \tag{3.14}$$

The locally generated replicas are the same as before and they are given by (3.2) and (3.3). The accumulated I_n Becomes:

$$I_n = \frac{1}{T} \int_{(n-1)T}^{nT} y(t) y_{I,n}(t)\, dt$$

$$= \frac{1}{T} \int_{(n-1)T}^{nT_i} \cos(\alpha_{0,n} t^2 + \omega_c t + \omega_{0,n} t + \phi_{0,n}) \cos(\omega_c t + \hat{\omega}_n t + \tilde{\phi}_n)\, dt$$

$$= \frac{1}{2T} \int_{(n-1)T}^{nT} \cos\left(\alpha_{0,n} t^2 + (\omega_{0,n} - \hat{\omega}_n)\, t + \phi_{0,n} - \tilde{\phi}_n\right)\, dt + \text{double freq term}$$

$$= \frac{1}{T\sqrt{\alpha_{0,n}}} \cos\left(\phi_{0,n} - \tilde{\phi}_n - \frac{(\omega_{0,n} - \hat{\omega}_n)^2}{4\alpha_{0,n}}\right) \mathrm{C}\left(\frac{\alpha_{0,n} t + \frac{(\omega_{0,n} - \hat{\omega}_n)}{2}}{\sqrt{\alpha_{0,n}}}\right)$$

$$\left. - \frac{1}{T\sqrt{\alpha_{0,n}}} \sin\left(\phi_{0,n} - \tilde{\phi}_n - \frac{(\omega_{0,n} - \hat{\omega}_n)^2}{4\alpha_{0,n}}\right) \mathrm{S}\left(\frac{\alpha_{0,n} t + \frac{(\omega_{0,n} - \hat{\omega}_n)}{2}}{\sqrt{\alpha_{0,n}}}\right) \right|_{(n-1)T}^{nT}$$

$$= \frac{1}{T\sqrt{\alpha_{0,n}}} \cos\left(\phi_{0,n} - \tilde{\phi}_n - \frac{(\omega_{0,n} - \hat{\omega}_n)^2}{4\alpha_{0,n}}\right) \cdot$$

$$\left[\mathrm{C}\left(\frac{\alpha_{0,n} nT + \frac{(\omega_{0,n} - \hat{\omega}_n)}{2}}{\sqrt{\alpha_{0,n}}}\right) - \mathrm{C}\left(\frac{\alpha_{0,n}(n-1)T + \frac{(\omega_{0,n} - \hat{\omega}_n)}{2}}{\sqrt{\alpha_{0,n}}}\right) \right]$$

$$- \frac{1}{T\sqrt{\alpha_{0,n}}} \sin\left(\phi_{0,n} - \tilde{\phi}_n - \frac{(\omega_{0,n} - \hat{\omega}_n)^2}{4\alpha_{0,n}}\right) \cdot$$

$$\left[\mathrm{S}\left(\frac{\alpha_{0,n} nT + \frac{(\omega_{0,n} - \hat{\omega}_n)}{2}}{\sqrt{\alpha_{0,n}}}\right) - \mathrm{S}\left(\frac{\alpha_{0,n}(n-1)T + \frac{(\omega_{0,n} - \hat{\omega}_n)}{2}}{\sqrt{\alpha_{0,n}}}\right) \right]$$

$$(3.15)$$

Where $C(x) = \int_0^x \cos t^2\, dt$ and $S(x) = \int_0^x \sin t^2\, dt$ are the Fresnel integrals. Further details and special properties of Fresnel integrals are included in Appendix A.

Using $\delta\tilde{\phi}_n = \phi_{0,n} - \tilde{\phi}_n$ yields to the following form of $G_I(\cdot)$

$$I_n = G_I^{(2)}(\delta\tilde{\phi}_n, \delta\hat{\omega}_n, \alpha_{0,n}) = \frac{1}{T\sqrt{\alpha_{0,n}}} \cos\left(\delta\tilde{\phi}_n - \frac{\delta\hat{\omega}_n^2}{4\alpha_{0,n}}\right) \cdot$$
$$\left[C\left(\frac{\alpha_{0,n}(n+1)T + \frac{\delta\hat{\omega}_n}{2}}{\sqrt{\alpha_{0,n}}}\right) - C\left(\frac{\alpha_{0,n}nT + \frac{\delta\hat{\omega}_n}{2}}{\sqrt{\alpha_{0,n}}}\right)\right]$$
$$- \frac{1}{T\sqrt{\alpha_{0,n}}} \sin\left(\delta\tilde{\phi}_n - \frac{\delta\hat{\omega}_n^2}{4\alpha_{0,n}}\right) \cdot$$
$$\left[S\left(\frac{\alpha_{0,n}(n+1)T + \frac{\delta\hat{\omega}_n}{2}}{\sqrt{\alpha_{0,n}}}\right) - S\left(\frac{\alpha_{0,n}nT + \frac{\delta\hat{\omega}_n}{2}}{\sqrt{\alpha_{0,n}}}\right)\right]$$
$$(3.16)$$

Similarly we derive Q_n as follows:

$$Q_n = \frac{1}{T}\int_{(n-1)T}^{nT} y(t)y_{Q,n}(t)\,dt$$
$$= \frac{1}{T}\int_{(n-1)T}^{nT_i} \cos(\alpha_{0,n}t^2 + \omega_c t + \omega_{0,n}t + \phi_{0,n}) \times -\sin(\omega_c t + \hat{\omega}_n t + \tilde{\phi}_n)\,dt$$
$$= \frac{1}{2T}\int_{(n-1)T}^{nT} \sin\left(\alpha_{0,n}t^2 + (\omega_{0,n} - \hat{\omega}_n)t + \phi_{0,n} - \tilde{\phi}_n\right)\,dt + \text{double freq term}$$
$$= \frac{1}{T\sqrt{\alpha_{0,n}}} \cos\left(\phi_{0,n} - \tilde{\phi}_n - \frac{(\omega_{0,n} - \hat{\omega}_n)^2}{4\alpha_{0,n}}\right) S\left(\frac{\alpha_{0,n}t + \frac{(\omega_{0,n}-\hat{\omega}_n)}{2}}{\sqrt{\alpha_{0,n}}}\right)$$
$$+ \frac{1}{T\sqrt{\alpha_{0,n}}} \sin\left(\phi_{0,n} - \tilde{\phi}_n - \frac{(\omega_{0,n} - \hat{\omega}_n)^2}{4\alpha_{0,n}}\right) C\left(\frac{\alpha_{0,n}t + \frac{(\omega_{0,n}-\hat{\omega}_n)}{2}}{\sqrt{\alpha_{0,n}}}\right)\Bigg|_{(n-1)T}^{nT}$$
$$= \frac{1}{T\sqrt{\alpha_{0,n}}} \cos\left(\phi_{0,n} - \tilde{\phi}_n - \frac{(\omega_{0,n} - \hat{\omega}_n)^2}{4\alpha_{0,n}}\right) \cdot$$
$$\left[S\left(\frac{\alpha_{0,n}nT + \frac{(\omega_{0,n}-\hat{\omega}_n)}{2}}{\sqrt{\alpha_{0,n}}}\right) - S\left(\frac{\alpha_{0,n}(n-1)T + \frac{(\omega_{0,n}-\hat{\omega}_n)}{2}}{\sqrt{\alpha_{0,n}}}\right)\right]$$
$$+ \frac{1}{T\sqrt{\alpha_{0,n}}} \sin\left(\phi_{0,n} - \tilde{\phi}_n - \frac{(\omega_{0,n} - \hat{\omega}_n)^2}{4\alpha_{0,n}}\right) \cdot$$
$$\left[C\left(\frac{\alpha_{0,n}nT + \frac{(\omega_{0,n}-\hat{\omega}_n)}{2}}{\sqrt{\alpha_{0,n}}}\right) - C\left(\frac{\alpha_{0,n}(n-1)T + \frac{(\omega_{0,n}-\hat{\omega}_n)}{2}}{\sqrt{\alpha_{0,n}}}\right)\right]$$
$$(3.17)$$

24

This yields to the following form of $G_Q(\cdot)$

$$Q_n = G_Q^{(2)}(\delta\tilde{\phi}_n, \delta\hat{\omega}_n, \alpha_{0,n}) = \frac{1}{T\sqrt{\alpha_{0,n}}} \cos\left(\delta\tilde{\phi}_n - \frac{\delta\hat{\omega}_n^2}{4\alpha_{0,n}}\right).$$
$$\left[S\left(\frac{\alpha_{0,n}(n+1)T + \frac{\delta\hat{\omega}_n}{2}}{\sqrt{\alpha_{0,n}}}\right) - S\left(\frac{\alpha_{0,n}nT + \frac{\delta\hat{\omega}_n}{2}}{\sqrt{\alpha_{0,n}}}\right) \right]$$
$$+ \frac{1}{T\sqrt{\alpha_{0,n}}} \sin\left(\delta\tilde{\phi}_n - \frac{\delta\hat{\omega}_n^2}{4\alpha_{0,n}}\right).$$
$$\left[C\left(\frac{\alpha_{0,n}(n+1)T + \frac{\delta\hat{\omega}_n}{2}}{\sqrt{\alpha_{0,n}}}\right) - C\left(\frac{\alpha_{0,n}nT + \frac{\delta\hat{\omega}_n}{2}}{\sqrt{\alpha_{0,n}}}\right) \right]$$
$$\text{(3.18)}$$

The integrals in (3.15) and (3.17) are evaluated using (A.9) and (A.10) respectively.

Furthermore, because the NCO model remains the same as in section 3.2.1 the phase continuity is maintained using $\tilde{\phi}_n$ as shown in equation (3.7).

The discriminator output used is again:

$$D_n = \text{atan}\left(\frac{Q_n + \eta_{Q,n}}{I_n + \eta_{I,n}}\right) \tag{3.19}$$

Hence, we have built a new PLL simulation model. Although it cannot simulate arbitrary dynamics, nevertheless for a constant acceleration, it has the advantage of accurately computing the I_n an Q_n outputs of the accumulate and dump procedure. This simulator was verified to exactly match the Intermediate Frequency (IF) model described in section 3.3 for zero jerk stress or higher order dynamics. One other use of this simulator is simulating the maximum allowed LOS acceleration stress for second order Loops.

Another interesting aspect for this part is observing the relation of dynamics to the noise behavior. In other words, we know that for third order loop that acceleration is transparent to the phase output. We also know that an allowable acceleration causes a constant phase shift. Therefore it is always thought that dynamics, a constant acceleration for instance, would only affect the mean whereas jitter is exclusively affected by noise (including oscillator noise). Verifying this analytically seems to be a tedious task. Hence, this simulator can be used for this purpose, and figure 3.6 reveals as expected, that acceleration is transparent to jitter.
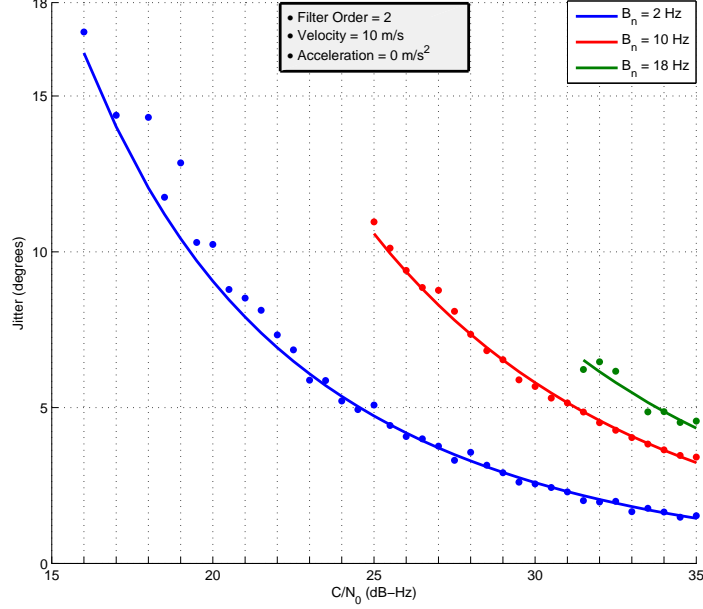
Figure 3.4: Measured and Theoretical Phase jitter an

3.2.3 C/N$_0$ and the Noise Power

In the previous two sections 3.2.1 and 3.2.2 $\eta_{I,n}$ and $\eta_{Q,n}$ represent two identical and independent additive white gaussian noise processes with variance σ_η^2. We now proceed finding the relation between σ_η^2 and C/N$_0(dB - Hz)$.

To start off we consider the original model then we trace it down into our model. We first assume that the amplitude A of the incoming signal is equal to unity. This will not harm the simulation model with the correct choice of σ_η^2 we are looking at. As provided in [1], the raw signal coming from the satellite having a white noise with one sided power spectral density of N_0 will yield to a noise $n_s(t)$ such that

$$n_s(t) = n_Q(t).\cos(\omega_{\mathrm{IF}}t) + n_I(t).\sin(\omega_{\mathrm{IF}}t) \tag{3.20}$$

The noise terms$n_c(t)$ and $n_s(t)$ in (3.20) have the same variance denoted σ_s^2. Moreover the variance of $n_s(t)$ is also equal to σ_s^2 because the multiplication with $\cos(\cdot)$ and $\sin(\cdot)$ equally split the power to half on each of the I and Q channels. Taking into consideration that the original signal has a power of $\frac{A^2}{2} = \frac{1}{2}$ results in

$$\sigma_s^2 = \frac{A^2}{2} \times \frac{N_0}{2} \times \frac{1}{T_s} = \frac{N_0}{4.T_s} \tag{3.21}$$

26
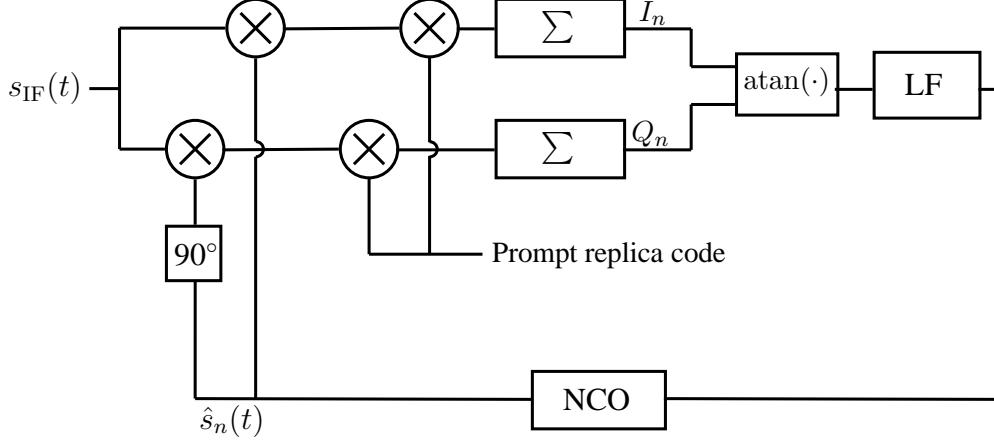
Figure 3.5: Intermediate frequency Costas carrier phase tracking loop

$$= \frac{1}{4.T_s. \cdot C/N_0} \quad (\text{rad}^2) \tag{3.22}$$

with T_s the sampling frequency of the incoming signal in the original IF tracking loop.

Nevertheless, in sections 3.2.1 and 3.2.2 the noise sources are modeled to be adding to the I_n and Q_n after the signal correlation process. With N being the number of samples during the correlation period the variance of the in-phase I_n and quadrature Q_n components of the correlation output can be computed, refereing to appendix B we get:

$$\sigma_{\eta,I}^2 = \sigma_{\eta,Q}^2 = \frac{2}{N}\sigma_s^2 = 2 \times \sigma_s^2 \times \frac{T_s}{T} = \frac{1}{2T \cdot C/N_0} \quad (\text{rad}^2) \tag{3.23}$$

This relation non surprisingly coincides with the results of [2] although the system is definition along with the approach used are different.

Figure 3.4 shows the jitter measurements of a second order PLL. The plot shows a match between the measured values and the theoretical values given by [3] in the following relation

$$\sigma_{\text{PLL}} = \frac{360}{2\pi}\sqrt{\frac{B_n}{\cdot C/N_0}\left(1 + \frac{1}{2T \cdot C/N_0}\right)} \quad (\text{deg}) \tag{3.24}$$

3.3 Intermediate Frequency Implementation

The Intermediate Frequency (IF) implementation follows the model of figure 3.5. This is in fact what is typically done in most receivers. The implementation is
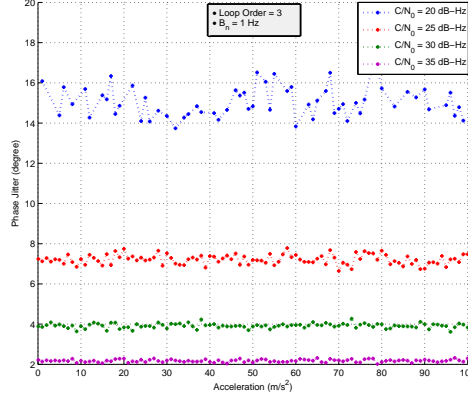
Figure 3.6: Phase Jitter vs Acceleration for a third order PLL

similar to the simulation model of section 3.2.2 in terms of the discriminator and the loop filter. However, in contrast to the simulation, this model implements the accumulate and dump as it is. In other words, it takes the sampled signal as input, not only the coefficients of its LOS dynamics polynomial. The signal is separately generated and could be an actual GPS IF signal for instance. Therefore, this model is exact and helps to accurately simulate a carrier tracking PLL with randomly varying dynamics. Although this model is the most accurate because it implements an actual Costas loop, in some cases of simulating very long input sequences, it is impractical due to the computationally demanding accumulate and dump stage.

3.4   Simulation and Results

At the first place consider the effect of a constant acceleration on the PLL. We suspect that although acceleration is transparent to a third order loop, high acceleration values could have a noise-like effect due to the attenuation they cause in the signal correlation step. Nevertheless, figure 3.6 shows that this effect does not exist for accelerations up to 100 m/s^2. It is obvious that the phase jitter is constant regardless how big the acceleration is. Moreover, if the mentioned effect was causing serious attenuation in the I and Q values, all the plots should have shown an increasing tendency with the same slope, clearly this is not the case. It is also possible that the third order loop filter which is aware of acceleration is counteracting for the attenuation effect automatically.

Secondly, we consider two different scenarios of random walk acceleration. The exact process describing the signal will be presented later in section 4.2 of chapter
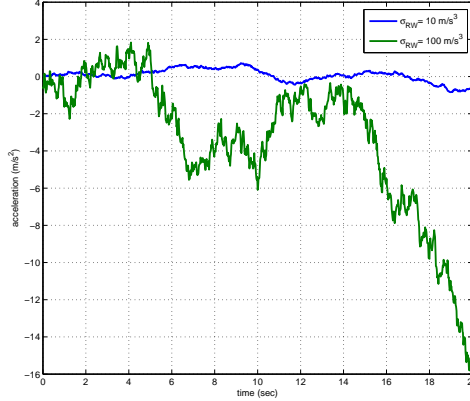
Figure 3.7: Low and high dynamics random walk acceleration profiles considered in simulations

4. The first scenario represents a low intensity of dynamics variation while the second represents a high intensity variation in dynamics, with the intensity metrics $\sigma_{RW} = 10$ m/s^3 and 100 m/s^3 respectively. The unit (m/s^3) belongs to the standard deviation of the with gaussian jerk causing this random walk. Please refer to appendix C for more details. The generated acceleration signals are shown in 3.7. It is important to mention that exactly the same two random walk acceleration profiles are used over the several simulation runs in order to guarantee fairness in the comparison with systems developed later in chapter 4.

Simulations of a third order PLL with different carrier to noise ratio C/N$_0$ and loop bandwidth B$_n$ values were carried for both random walk scenarios. The simulations took place over 100 runs and then results were averaged. However, in some low C/N$_0$ cases fewer values were able to maintain lock, this can be seen in the non conforming plots of low C/N$_0$. Figures 3.8 and 3.9 summarize these results. Next, the results were further used to find the optimal noise bandwidth which can be found in figure 3.10. This approach was previously used by [4]. As also observed by the author, one can notice that the optimal loop bandwidth is linearly increasing with C/N$_0$. Nevertheless, it is not the case for some low C/N$_0$ for the lack of measurements. Finally figure 3.11 shows the best possible jitter performance of the third order PLL in each of the two dynamics scenarios. It can be seen in this figure that with the highly changing dynamics environment the performance of the PLL drops down. In fact, in low dynamics the loop abides to the 15° 3-sigma rule for signals no weaker then 21 dB-Hs whereas under high dynamic the PLL needs at least 25 dB-Hz. This result is interesting in the sense that rapid changes in the dynamics environment have an effect similar to noise. In

other words, the higher the dynamics the higher is the optimal noise bandwidth. Hence, although the noise bandwidth is optimally and simultaneously adapting to both the random noise and the random variation in the signal dynamics, more noise is permitted by the loop filter and accordingly the PLL witnesses additional phase jitter cause by this combined effect.
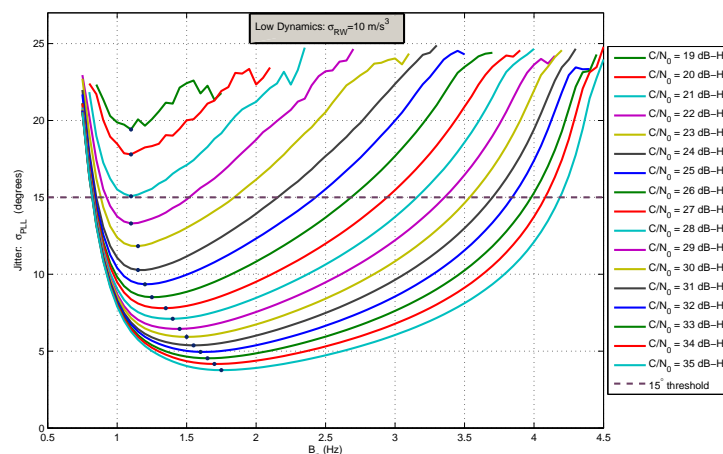
Figure 3.8: PLL Jitter for several B_n and C/N_0 values under low dynamics random walk acceleration for a third order PLL
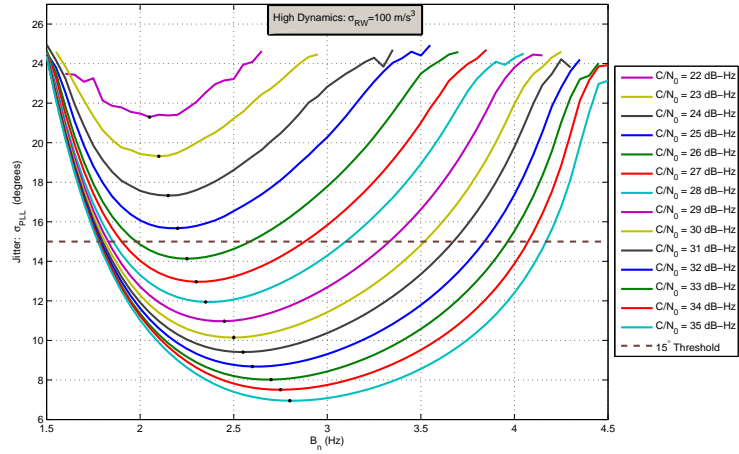
Figure 3.9: PLL Jitter for several B_n and C/N_0 values under High dynamics random walk acceleration for a third order PLL
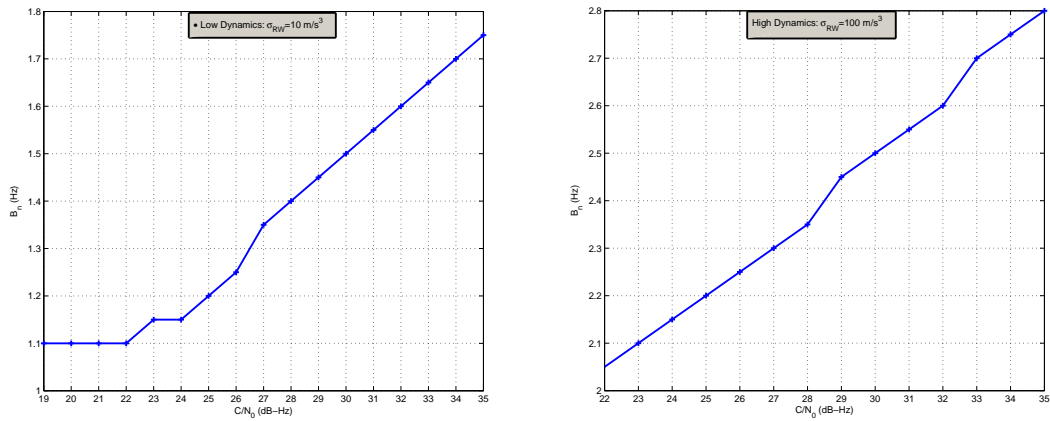
Figure 3.10: Optimal Loop Bandwidth B_n vs. C/N_0 for the low (left) and high (right) dynamics profiles for a third order PLL
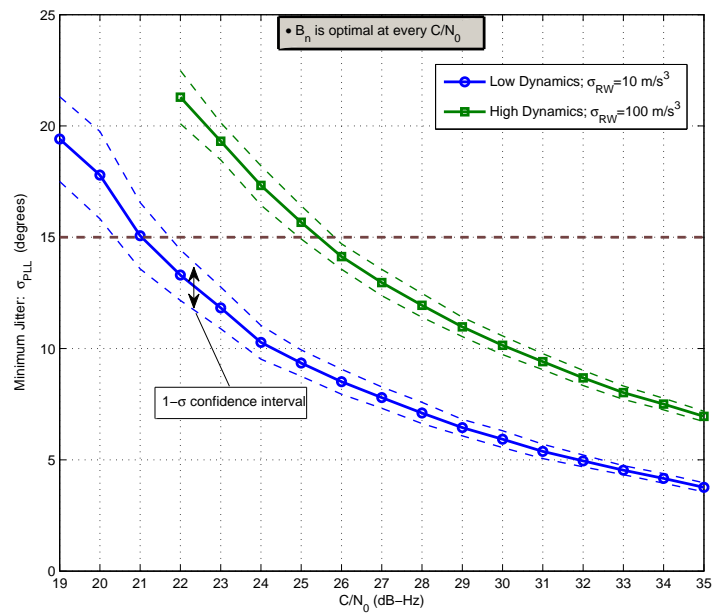
Figure 3.11: Minimum PLL jitter. The optimal value of B_n depending on the C/N_0 for a third order PLL

Chapter 4

Extended Kalman Filter Tracking

In this chapter we present a different approach to the tracking problem, that is the Extended Kalman filter solution. We first present a description of the LOS signal dynamics process. Once the system is defined in section 4.2 we proceed with the tracking loop design.

The Kalman Filter tracking loop is constituted from three components. The first is the measurement component which implements one of several possible measurement models. In the measurement stage needed information about the signal are extracted. Precisely, the exact integrate and dump process used in PLLs is adopted here. The measured I_n and Q_n, or a combination of them, serve then as a measurement to be fed into the state estimation block.

The second component is the state estimation block. One key feature of the Kalman filter state estimation is its real time iterative approach. It works by predicting the next state of the system based on the process description it is aware of while making use of the measurement to correct the predicted state. The filter decides in real time the level of trust given to each prediction and correction. This trust weighting factor is decided by the Kalman gain. This gain factor is designed to minimize the mean square error in the state estimate, making the Kalman filter a very suitable solution to the tracking problem. In other words, if we consider the phase of the incoming signal to be one of the states describing the system in hand, then this strictly means that the mean square phase error is minimum. This however requires a perfect knowledge of the process description. In section 4.3 we present a first order Extended Kalman Filter (EKF) state estimation. Several forms of the filter are shown depending on the chosen measurement model. We then show the second order filter as well, which uses a second order Taylor series expansion of the measurement model for more accuracy in the correction stage.

The third component of the EKF tracking loop is the control law. The control law is a factor in the behavior of the loop. It is mainly critical for the stability of the loop. Furthermore an appropriate choice of the control gain matrix or
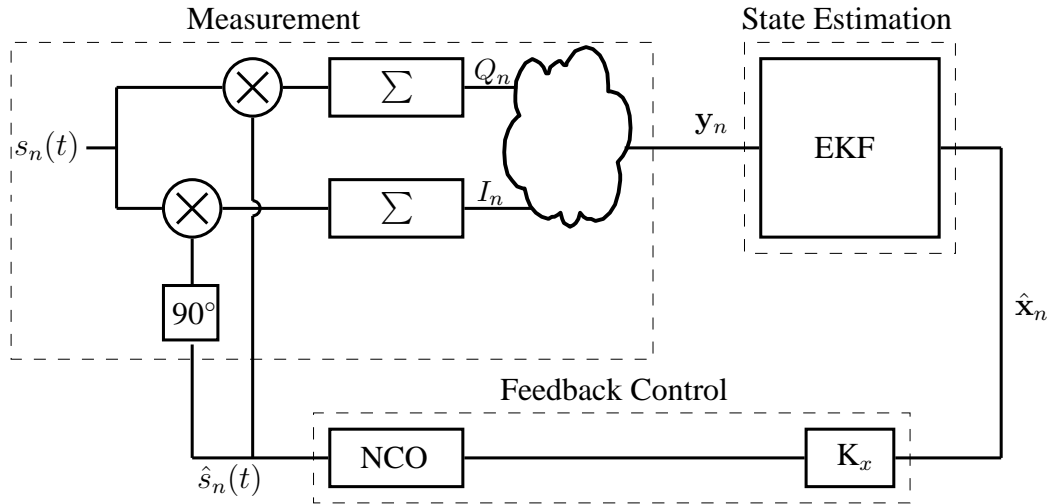
Figure 4.1: Extended Kalman Filter Loop Model. The cloud represents different combinations of I_n and Q_n, these are $\mathbf{y}_n = Q_n$, $\mathrm{atan}(\frac{Q_n}{I_n})$ or $[I_n \quad Q_n]^T$

equivalently, an appropriate pole placement will determine the characteristics of the loop such the maximum overshoot and settle time. Moreover, the control law will vary depending on the NCO order.

4.1 Background

The topic of Kalman filter tracking of the carrier frequency and phase originates back to the 1980's. Using the results of [5] the authors of [6] carry a comparison for different carrier frequency estimation techniques for high dynamics trajectories. In this work, the systems subject of comparison are: an approximate maximum likelihood, an Extended Kalman filter, a cross product automatic frequency control loop and a PLL. In what matters to our research, the PLL outperforms the EKF for carrier to noise ratios above 26 dB-Hz while the latter shows lower frequency estimation error near the region of 23 dB-Hz where they both lose lock.

A Hybrid Minmax Kalman tracking filter was devised by [7]. This work tackles the problem that a Kalman filter requires a perfect knowledge about the noise from the designer. It is solved by weighting its gain with another gain factor provided by the Minmax filter. As the latter does not require any prior knowledge about the noise, the hybrid combination, although has worse overall tracking performance is claimed to be a good compromise.

More recent research in the subject was done by M. Psiaki in [8] and [9]. The authors present a combined code and carrier tracking loop based on the

extended Kalman filter. The measurements used in the carrier tracking EKF for state correction update is the atan(·) discriminator output originally used in Costas Loop. While the measurement model is considered to be the average phase in one integration integral. This combination forms a likelihood function that is iteratively minimized by the EKF. The adopted EKF takes the iterated and Square root form. The iterated filter helps reducing the linearization error as it iteratively refines the measurement estimate based on the corrected estimate of the states. The Square root filter however was adopted as it is more computationally robust. In addition to code and carrier tracking the work was also extended to detect bit transition using a special probabilistic (bayesian) treatment.

Similar work was presented in [10] with the use of the Linear Qdratic Regulator (LQR) to implement the EKF. The filter was compared to the traditional PLL tracking method. The work concludes that EKF tracking provides some benefits over PLL tracking. The ground that brings the two systems into a valid comparison is a steady state noise equivalent bandwidth metric suggested by the authors.

Another code and carrier tracking filter was studied and developed by N. Ziedan et. al. in [11]. A square root implementation was adopted as well to circumvent numerical errors associated with the Kalman filter. A first and a second order EKF tracking methods are presented. The measurements considered in this work is the accumulated Q for the first order EKF and both I and Q values for the second. Along with the signal dynamics the model also estimates the amplitude of the incoming signal and has the ability to adjust the integration time. The measurement model is a simplified one that only considers the amplitude estimate and the phase error estimate. Furthermore the Jacobian and Hessian matricides used to calculate the first and second order components of the measurement estimate take a time invariant form. In 4.3.1 some of these approaches will be considered and compared.

4.2 Process Description

The process describing the signal dynamics takes the form of state transitions driven by a discrete-time white noisy disturbance:

$$\mathbf{x}_{n+1} = \Phi \mathbf{x}_n + \nu_n \tag{4.1}$$

The signal phase, frequency and frequency change rate are nothing but the scaled distance, velocity and acceleration respectively. Therefore, the signal phase and its derivatives are the appropriate choice of states that accurately model the LOS dynamics. Let us then consider the state vector to be $\mathbf{x}_n = [\phi_n \quad \omega_n \quad \alpha_n]^T$.

Since consecutive components of the state vector are integrals of the succeeding ones, repeated integration over the sampling period yields to

$$\alpha_{n+1} = \alpha_n + \nu_{j,n} \tag{4.2}$$

$$\omega_{n+1} = \omega_n + T\alpha_n + \nu_{\alpha,n} \tag{4.3}$$

$$\phi_{n+1} = \phi_n + T\omega_n + \frac{T^2}{2}\alpha_n + \nu_{\omega,n} \tag{4.4}$$

Where

$$\nu_{k,n} = \int_{(n-1)T}^{nT} \frac{(nT-\tau)^{3-k}}{(3-k)!} Y(\tau) \, d\tau, \qquad k = 1, 2, 3 \text{ standing for } \omega, \alpha \text{ and } j \tag{4.5}$$

The subscript j denotes the jerk dynamics while $Y(t)$ denotes the third derivative of the continuous version of the phase. Assuming $Y(t)$ is a zero-mean white process with one-sided power spectral density N_j, or equivalently that the disturbance is a zero-mean white Gaussian jerk stress, we get

$$E[\nu_{j,n}^2] = \frac{N_j T}{2} = \sigma_j^2 T^2 \tag{4.6}$$

Using equations (4.2) through (4.5) we get process transition matrix Φ. Furthermore, we show the resulting process disturbance covariance matrix $Q_{\nu\nu}$. The exact derivation of $Q_{\nu\nu}$ is however shown in Appendix C.

$$\Phi = \begin{bmatrix} 1 & T & T^2/2 \\ 0 & 1 & T \\ 0 & 0 & 1 \end{bmatrix} \tag{4.7}$$

$$Q_{\nu\nu} = \sigma_j^2 \begin{bmatrix} T^6/20 & T^5/8 & T^4/6 \\ T^5/8 & T^4/3 & T^3/2 \\ T^4/6 & T^3/2 & T^2 \end{bmatrix} \tag{4.8}$$

4.3   EKF State Estimation

The first order extended Kalman filter is described as follows

EKF time update equation *(a priori state prediction)*

$$\hat{\mathbf{x}}_n^- = \Phi\hat{\mathbf{x}}_{n-1} + \Gamma\mathbf{u}_{n-1} \tag{4.9}$$

$$P_n^- = \Phi P_{n-1}\Phi^T + Q_{\nu\nu} \tag{4.10}$$

$$K_n = P_n^- H_n^T (H_n P_n^- H_n^T + R_{\vartheta\vartheta})^{-1} \qquad (4.11)$$

$$\hat{\mathbf{x}}_n = \hat{\mathbf{x}}_n^- + K_n(\mathbf{z}_n - h(\hat{\mathbf{x}}_n^-, 0)) \qquad (4.12)$$

$$P_n = (I - K_n H_n)P_n^- \qquad (4.13)$$

$$\mathbf{u}_n = -K_x \hat{\mathbf{x}}_n \qquad (4.14)$$

$\mathbf{x}$: is the state vector. Even though one may choose the states to be the same as the ones describing the process shown in section 4.2, we will consider here the following state vector

$$\mathbf{x}_n = \begin{bmatrix} \delta\phi_n \\ \delta\omega_n \\ \delta\alpha_n \end{bmatrix} = \begin{bmatrix} \phi_n - \phi_{\text{NCO},n} \\ \omega_n - \omega_{\text{NCO},n} \\ \alpha_n - \alpha_{\text{NCO},n} \end{bmatrix} \qquad (4.15)$$

Where $\phi_{\text{NCO},n}$, $\omega_{\text{NCO},n}$ and $\alpha_{\text{NCO},n}$ correspond to the signal replica generated by the NCO. More precisely, they describe it at the time instance exactly at the beginning of the nth epoch. Thus, as we have a perfect knowledge of the NCO signal, the state vector shown in (4.15) is sufficient to describe our dynamics system.

$h(\mathbf{x}, \mathbf{u})$: is the measurement function mapping the measurement $\mathbf{z}_n$ into the state space as follows

$$\mathbf{z}_n = h(\mathbf{x}_n, \mathbf{u}) + \vartheta_n \qquad (4.16)$$

H_n: is the linearized measurement model mapping the states into the measurement space. The subscript n is used to emphasize that H can be time varying. In general, where $h(\mathbf{x}, \mathbf{u})$ is nonlinear, H_n is the Jacobian matrix of $h(\mathbf{x}, \mathbf{u})$ evaluated at the predicted states $\hat{\mathbf{x}}_n^-$

$$H_n = \begin{bmatrix} \dfrac{\partial h_1(\mathbf{x}, \mathbf{u})}{\partial x_1} & \cdots & \dfrac{\partial h_1(\mathbf{x}, \mathbf{u})}{\partial x_n} \\ \vdots & \ddots & \vdots \\ \dfrac{\partial h_m(\mathbf{x}, \mathbf{u})}{\partial x_1} & \cdots & \dfrac{\partial h_m(\mathbf{x}, \mathbf{u})}{\partial x_n} \end{bmatrix} \Bigg|_{(\mathbf{x},\mathbf{u})=(\hat{\mathbf{x}}_n^-, 0)} \qquad (4.17)$$

In some cases the mapping function $h(\mathbf{x}, 0)$ can be linearized, if that is the case the H matrix is used for measurement prediction. The measurement update equation (4.12) becomes

$$\hat{\mathbf{x}}_n = \hat{\mathbf{x}}_n^- + K_n(\mathbf{z}_n - H_n \hat{\mathbf{x}}_n^-) \qquad (4.18)$$

$$(4.19)$$

u: is the NCO control input

Γ: is the control driving matrix, which maps the effect of the control input into the state space.

Note that **u** and Γ will be tackled later in section 4.5

$Q_{\nu\nu}$: is the process disturbance covariance matrix given by (4.8).

$R_{\vartheta\vartheta}$: is the measurement noise covariance matrix which will be defined later, differently for every measurement model.

4.3.1   Measurement Models

Several measurement models have been previously used, most widely adopted is $\mathbf{z}_n = \text{atan}\left(\frac{I_n}{Q_n}\right)$ mainly for two reasons. These are the simplicity of a single measurement model and the similarity with the conventional PLL it gives to the problem. Another measurement model could be simply Q. This model is also simple and treats $\mathbf{z}_n = Q_n$ as the error between the signal and the replica to be controlled down to zero. The most comprehensive measurement model is $\mathbf{z}_n = [I_n \ \ Q_n]^T$. If the state estimator is designed appropriately, this measurement model guarantees the most information about the incoming signal. Indeed, because the two aforementioned models measure either part of the available information or a non-linear combination of it, that is the atan operation. In sections 4.3.1.1, 4.3.1.2 and 4.3.1.3 we describe these models, each with its corresponding measurement estimate scheme needed for state estimation.

4.3.1.1   The Quadrature Component Q_n-only Measurement Model

Although a mapping from the state space into Q_n was derived in the previous chapter, in equation (3.11) or (3.18). This model, adopted in the carrier tracking EKF described in [11] assumes $\hat{\mathbf{z}}_n = [\hat{Q}_n] = \delta\hat{\phi}_n^-$. This leads to a time invariant $H = \begin{bmatrix} 1 & 0 & 0 \end{bmatrix}$

Therefore the measurement update equation (4.12) becomes

$$\hat{\mathbf{x}}_n = \hat{\mathbf{x}}_n^- + K_n(Q_n - \delta\hat{\phi}_n^-) \tag{4.20}$$

This assumption implicitly says that steering $\delta\phi$ to zero is equivalent to steering the quadrature component to zero, as this will shift all the power to the in-phase channel. The assumption can be expressed using the following approximations

$$\hat{Q}_n \approx \sin\ \delta\hat{\phi}_n^- \approx \delta\hat{\phi}_n^- \tag{4.21}$$

The measurement covariance matrix is simply as scalar given by (3.23) in the form $R_{\vartheta\vartheta} = \sigma_{\eta,Q}$.

This model is highly simple as it does not require extra computational burden for computing $\hat{\mathbf{x}}_n^-$ and H_n. However it is expected to have a poor performance.

4.3.1.2 The Average Phase Difference Measurement Model

$$\mathbf{z}_n = Q_n \tag{4.22}$$

$$\mathbf{z}_n = \mathrm{atan}\left(\frac{Q_n}{I_n}\right) \tag{4.23}$$

This model considers a single measurement that is $\hat{\mathbf{z}}_n = \overline{[\Delta\phi]} \approx \mathrm{atan}\left(\frac{Q_n}{I_n}\right)$. where $\overline{\Delta\phi}$ represents the average phase difference over the whole integration interval n.

The predicted measurement $\hat{\mathbf{z}}_n$ is then

$$\hat{\mathbf{z}}_n = \overline{\Delta\phi} = \delta\hat{\phi}_n^- + \frac{T}{2}.\delta\hat{\omega}_n^- + \frac{T^2}{6}.\delta\hat{\alpha}_n^- \tag{4.24}$$

This yields to the following form of the measurement update equation

$$\hat{\mathbf{x}}_n = \hat{\mathbf{x}}_n^- + K_n\left(\mathrm{atan}\left(\frac{Q_n}{I_n}\right) - H\hat{\mathbf{x}}_n^-\right) \tag{4.25}$$

$$\text{with } H = \begin{bmatrix} 1 & \dfrac{T}{2} & \dfrac{T^2}{6} \end{bmatrix} \tag{4.26}$$

The relation between the measurement and C/N_0 also used by [10], is based on (3.24) provided in [2] which determines the variance of the output of an $\mathrm{atan}(\cdot)$ discriminator as:

$$R_{\vartheta\vartheta} = \sigma_{\delta\phi}^2 = \frac{1}{2T \cdot C/N_0}\left(1 + \frac{1}{2T \cdot C/N_0}\right) \quad \mathrm{rad}^2 \tag{4.27}$$

This model is similar to the previous one in the sense that a single measurement is considered. In addition, H is also time invariant. Nevertheless, this model is expected to have a better performance as it has better approximation for the measurement prediction $\hat{\mathbf{z}}_n$.

4.3.1.3 The I_n and Q_n Measurement Model

In this section we will consider the raw measurement $\mathbf{z}_n = \begin{bmatrix} I_n & Q_n \end{bmatrix}^T$ without any prior manipulation or simplifications such the treatments showed in sections 4.3.1.1 and 4.3.1.2. Indeed using the raw measurement leaves us with the highest possible degrees of freedom in order to develop a measurement model that accurately defines $h(\mathbf{x}, \mathbf{u})$.

This measurement model is highly inspired from sections 3.2.1 and 3.2.2, where in fact using the functions $G_I(\cdot)$ and $G_Q(\cdot)$ define the state-to-measurement mapping functions as follows

$$h(\hat{\mathbf{x}}_n^-, 0) = \begin{bmatrix} G_I(\hat{\mathbf{x}}_n^-) \\ G_Q(\hat{\mathbf{x}}_n^-) \end{bmatrix} \tag{4.28}$$

Additionally, the Jacobian matrix H_n is to be calculated using (4.17). And the measurement update equation becomes:

$$\hat{\mathbf{x}}_n = \hat{\mathbf{x}}_n^- + K_n \left(\begin{bmatrix} I_n \\ Q_n \end{bmatrix} - \begin{bmatrix} G_I(\hat{\mathbf{x}}_n^-) \\ G_Q(\hat{\mathbf{x}}_n^-) \end{bmatrix} \right) \tag{4.29}$$

The measurements will have a variance $\sigma_{\eta,I}$ and $\sigma_{\eta,Q}$ previously provided in (3.23), and the measurement noise covariance matrix will be

$$R_{\vartheta\vartheta} = \begin{bmatrix} \sigma_{\eta,I} & 0 \\ 0 & \sigma_{\eta,Q} \end{bmatrix} \tag{4.30}$$

In the following two possibilities to evaluate $h(\cdot)$ and H_n are described. The first represents the mapping in terms of the first two states whereas the second describe it in terms of all three states.

The Traditional Model: Without Acceleration A simple measurement model, used in [x], only relies on the relation of the measurements I_n and Q_n to the phase error $\delta\hat{\phi}_n$, that is

$$\hat{\mathbf{z}}_n = \begin{bmatrix} \cos \delta\phi_n^- \\ \sin \delta\phi_n^- \end{bmatrix} \tag{4.31}$$

with

$$H_n = \begin{bmatrix} -\sin \delta\phi_n^- & 0 & 0 \\ \cos \delta\phi_n^- & 0 & 0 \end{bmatrix} \tag{4.32}$$

We, however, provide an equivalent but more exact model using the following

$$\hat{\mathbf{z}}_n = \begin{bmatrix} G_I^{(1)}(\delta\hat{\phi}_n^-, \delta\hat{\omega}_n^-) \\ G_Q^{(1)}(\delta\hat{\phi}_n^-, \delta\hat{\omega}_n^-) \end{bmatrix} \tag{4.33}$$

where $G_I^{(1)}(\cdot)$ and $G_Q^{(1)}(\cdot)$ are derived in (3.10) and (3.11) respectively.

The resulting H_n will be

$$H_n = \begin{bmatrix} \dfrac{\partial G_I^{(1)}(\delta\phi, \delta\omega)}{\partial\delta\phi} & \dfrac{\partial G_I^{(1)}(\delta\phi, \delta\omega)}{\partial\delta\omega} & 0 \\ \dfrac{\partial G_Q^{(1)}(\delta\phi, \delta\omega)}{\partial\delta\phi} & \dfrac{\partial G_Q^{(1)}(\delta\phi, \delta\omega)}{\partial\delta\omega} & 0 \end{bmatrix}_{\delta\hat\phi_n^-, \delta\omega\omega_n^-}$$

$$= \begin{bmatrix} -\sin\left(\delta\hat\phi_n^- + \delta\hat\omega_n^- \cdot \tfrac{T}{2}\right) & -\tfrac{T}{2}\cdot\sin\left(\delta\hat\phi_n^- + \delta\hat\omega_n^- \cdot \tfrac{T}{2}\right) & 0 \\ \cos\left(\delta\hat\phi_n^- + \delta\hat\omega_n^- \cdot \tfrac{T}{2}\right) & \tfrac{T}{2}\cdot\cos\left(\delta\hat\phi_n^- + \delta\hat\omega_n^- \cdot \tfrac{T}{2}\right) & 0 \end{bmatrix} \tag{4.34}$$

where for simplicity the multiplier 'sinc $(\delta\hat\omega_n T)$' term was dropped because it is very close to one.

This measurement model imposes higher computational burden than the preceding ones because H_n is computed in real-time . Nevertheless this method is supposed to show better noise performance than those using a single measurement.

The Enhanced Model: With Acceleration   This measurement model is derived to be the most accurate among all other models shown in previous sections. Similarly to the model of 4.3.1.3, it uses the raw I_n and Q_n. Moreover, the estimated third state, namely the estimated acceleration $\delta\phi_n^-$ is also used in the measurement update. In other words

$$\hat{\mathbf{z}}_n = \begin{bmatrix} G_I^{(2)}(\delta\hat\phi_n^-, \delta\hat\omega_n^-, \delta\hat\alpha_n^-) \\ G_Q^{(2)}(\delta\hat\phi_n^-, \delta\hat\omega_n^-, \delta\hat\alpha_n^-) \end{bmatrix} \tag{4.35}$$

where $G_I^{(2)}(\cdot)$ and $G_Q^{(2)}(\cdot)$ are derived in (3.16) and (3.18) respectively.

Note that $\delta\hat\phi_n = \delta\tilde\phi_n$ in this case. This is correct if we consider the integration bounds to be zero to T. Indeed, this applies to the case here because the estimated states are ready at the beginning of every integration period. This guarantees that the effects of the signal dynamics on correlation to manifest only within that period. For the same reason, it is also important to tweak equations (3.16) and (3.18) setting the time arguments of the Fresnel integrals to 0 and T instead of $(n-1)T$ and nT respectively.

The resulting H_n will be

$$H_n = \begin{bmatrix} \dfrac{\partial G_I^{(1)}(\delta\phi, \delta\omega, \delta\alpha)}{\partial\delta\phi} & \dfrac{\partial G_I^{(1)}(\delta\phi, \delta\omega, \delta\alpha)}{\partial\delta\omega} & \dfrac{\partial G_I^{(1)}(\delta\phi, \delta\omega, \delta\alpha)}{\partial\delta\alpha} \\ \dfrac{\partial G_Q^{(1)}(\delta\phi, \delta\omega, \delta\alpha)}{\partial\delta\phi} & \dfrac{\partial G_Q^{(1)}(\delta\phi, \delta\omega, \delta\alpha)}{\partial\delta\omega} & \dfrac{\partial G_Q^{(1)}(\delta\phi, \delta\omega, \delta\alpha)}{\partial\delta\alpha} \end{bmatrix}_{\delta\hat\phi_n^-, \delta\omega\omega_n^-, \delta\omega\alpha_n^-} \tag{4.36}$$

Q-only	the model using Q only as a measurement.
atan($\cdot$)	the model using the atan output as a measurement.
I&Q-a	the model using both I and Q only as a measurement with $G^{(1)}(\cdot)$ mapping which does <u>not</u> consider the acceleration effect.
I&Q-b	the model using both I and Q only as a measurement with $G^{(2)}(\cdot)$ mapping which does consider the acceleration effect.

Table 4.1: List of naming conventions of the presented measurement models
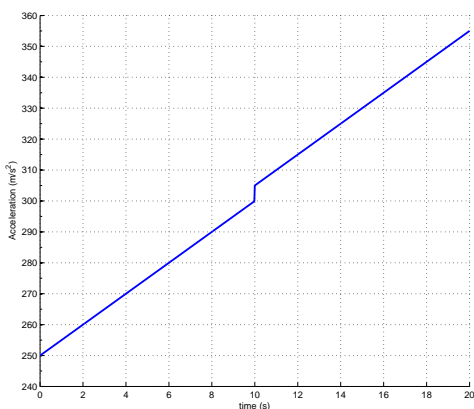
Figure 4.2: Acceleration scenario
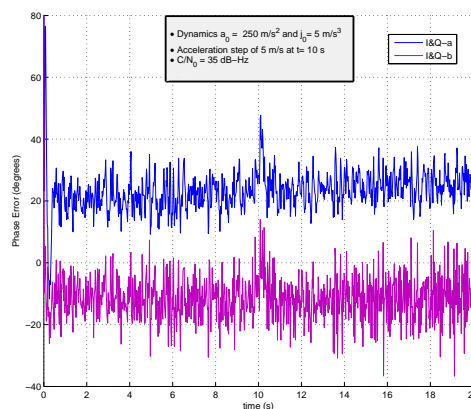
Figure 4.3: Phase Error of the I&Q-a and I&Q-b

Refer to appendix D for the exact form of H_n.

This filter is the highly complex compared to the previous ones, not only because H_n is computed in real time but also because of the excessive need to numerically evaluate the Fresnel integrals. Nevertheless, it is supposed to show an excellent performance compared to previously described ones.

4.3.2 Comparison of Measurement Models

In this section we will show comparison results of the several measurement models. The parameters related to the control law, discussed later in 4.5, are equivalent in all models. Moreover, a list of abbreviations making it easier to refer to the models is shown in table 4.1.

Figure 4.2 shows a devised high dynamic scenario used to compare the measurement models "I&Q-a" and "I&Q-b". The phase error is shown in figure 4.3. It can be seen that the enhanced model show a smaller phase bias initially caused by the jerk. In fact, the mean phase error is $\theta_e \simeq 10°$ whereas the first model
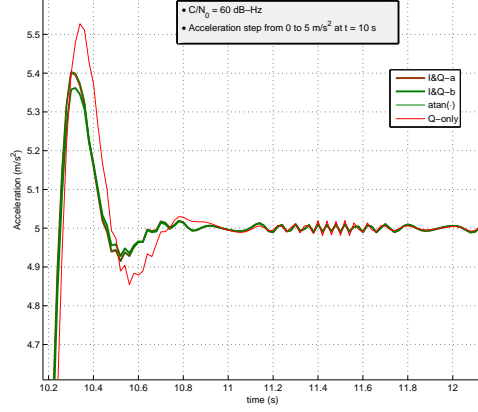
Figure 4.4: An acceleration step response at very high C/N$_0$
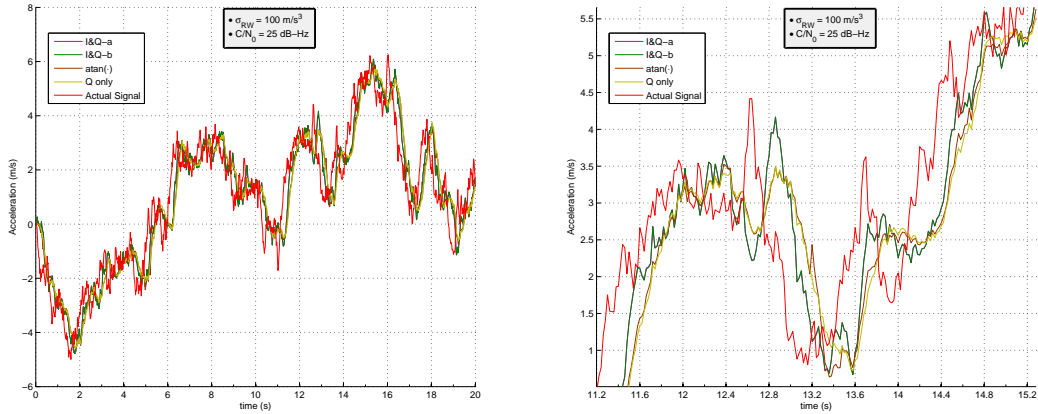
Figure 4.5: Random walk acceleration and the estimated acceleration by the different systems

shows a phase bias of $\theta_e \simeq 20°$. On the other hand the enhanced system shows a slightly larger jitter value. As can be seen in the figure, the error has a bigger variance in the case of "I&Q-b". Numerical values for this scenario where calculated over repeated simulations and the result is a jitter of $\sigma_\phi = 6.81°$ for "I&Q-a" and a $\sigma_\phi = 7.64°$ for "I&Q-b". This slight deterioration in performance is the price paid for using the sophisticated measurement model as it increases the numerical instabilities and linearization errors of the EKF based on the Fresnel integrals. Nevertheless, in this specific scenario, applying the 3-sigma rule yields that the enhanced system maintains a lock within the desired threshold of $45°$ whereas the
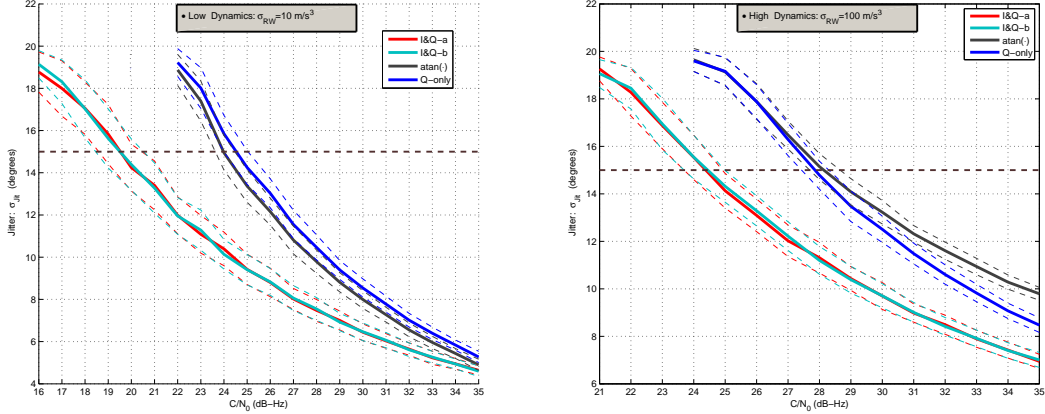
Figure 4.6: Phase jitter vs. C/N_0 for the measurement models with the low (left) and high (right) dynamics profiles

system that ignores the effect of acceleration in its measurement estimate fails to abide to this threshold. It is also important to mention that all other systems failed to maintain lock in this scenario.

The response of the several models was studied with an acceleration step of 5 m/s^2 at a very high carrier to noise ratio. Figure 4.4 shows that the EKF that uses the Q-only measurement model is performing the worst while the atan($\cdot$) show a similar performance to I&Q-a whereas the best performance, thanks to including the acceleration estimate in the measurement mapping, is for I&Q-b.

A more general simulation was carried using an acceleration random walk signal. The generation of the random signal follows the process described in 4.2. Moreover the assumed jerk standard deviation leading to the random walk acceleration shown figure 4.5 is $\sigma_j = 100$ m/s^3. All described systems maintain lock, nevertheless one can easily observe from the plots that the I&Q measurement models show the higher responsiveness in estimating the acceleration. This difference translate to a better jitter performance of these models when compared to the Q-only and the atan($\cdot$) models. A thorough jitter analysis will be provided in the next paragraph. This result can be justified by simply arguing that a two measurements input guarantees to the EKF, a better measurement update than would a single measurement input consisting to some combination of the two measurement we started with. This will not be true however unless the state-to-measurement mapping used by the EKF is good enough in the I&Q case, which we believe is true for both presented I&Q model. In contrast to (deterministic) scenario discussed above, the difference between the two I&Q models cannot be seen in this scenario for two reasons. This first is that the dynamics are not high

enough to emphasize it. Second, and most importantly, the bias θ_e caused by the randomly varying dynamics is also random and averaging it over the whole time frame of the simulation would be misleading.

Finally, a thorough simulation of 100 repeated runs is conducted using the exact two random walk acceleration profiles used in 3.4 and shown in fiure 3.7. The purpose of this simulation is to compare the measurement models in terms of their effect on phase jitter. Figure 4.6 summarizes the results. As expected, the models with dual measurements I&Q show the best performance. Moreover, I&Q-a and I&Q-b have an equivalent jitter performance. This point was analyzed previously where the gain of using I&Q-b is reducing the phase bias θ_e caused by high dynamics whereas the jitter is supposed to be of a slight disadvantage to the enhanced I&Q-b model. The Q-only measurement model shows the least performance in the low dynamics scenario. This result is expected considering its single approximation-based measurement model. Furthermore, the performance of the atan($\cdot$) model show a severe degradation with the increased dynamics. In theory this model is expected to remain better than Q-only model since it has a Costas like structure and make more accurate phase estimate than the latter. It is suspected however that this inconsistency is caused by the choice of the noise covariance value $\sigma_{\delta\phi}$ which was adopted from [10]. In fact, when comparing equation (3.24) to equation (4.27) one can notice that the chosen B_n parameter do not take into consideration any equivalent B_n used by the control law. The control law discussion will be carried however in section 4.5. Furthermore, for the all measurement models the jitter performance is degraded with higher intensity of the varying dynamics.

4.4   Second Order EKF

In this section we discuss a second order Kalman filter developed for the purpose of minimizing the linearization error of the mapping function $h(\mathbf{x}, \mathbf{u})$. Just as the first order filter, the second order EKF make use of the Taylor series expansion of $h(\cdot)$ around $\hat{\mathbf{x}}n^-$. But in contrast to the first order filter, the second order EKF makes use of the second order differential element as well. This can expressed as

$$h(\mathbf{x}_n, \mathbf{u}_n) = h(\hat{\mathbf{x}}_n^-, \mathbf{u}_n) + \left.\frac{\partial h}{\partial \mathbf{x}}\right|_{\hat{\mathbf{x}}_n^-}(\mathbf{x}_n - \hat{\mathbf{x}}_n^-) + \frac{1}{2}\sum_{i=1}^{m}\epsilon_i(\mathbf{x}_n - \hat{\mathbf{x}}_n^-)^T \left.\frac{\partial^2 h}{\partial \mathbf{x}^2}\right|_{\hat{\mathbf{x}}_n^-}(\mathbf{x}_n - \hat{\mathbf{x}}_n^-)$$

$$= h(\hat{\mathbf{x}}_n^-, \mathbf{u}_n) + H_n(\mathbf{x}_n - \hat{\mathbf{x}}_n^-) + \frac{1}{2}\sum_{i=1}^{m}\epsilon_i(\mathbf{x}_n - \hat{\mathbf{x}}_n^-)^T D_{i,n}(\mathbf{x}_n - \hat{\mathbf{x}}_n^-)$$

$$(4.37)$$

Where $m = 2$ is the number of measurements, $\epsilon_1 = [1 \quad 0]^T$ and $\epsilon_2 = [0 \quad 1]^T$. With $D_{i,n}$ being the Hessian matrices of $h(\mathbf{x}_n)$. Note here that although we consider the more exact form of $h(\cdot)$ given in (4.28) with the $G_I^{(2)}(\cdot)$ and $G_Q^{(2)}(\cdot)$. We will consider, for simplicity, in deriving $D_{i,n}$ the simpler form of $h(\cdot)$ given by $G_I^{(1)}(\cdot)$ and $G_Q^{(1)}(\cdot)$. This will in other words, neglect the acceleration effect in the second order term of the Taylor expantion of $h(\cdot)$ while keeping it for the first order. This assumption is expected to maintain the gain coming from reducing the linearization error. As a result we will end up with the following forms of $D_{i,n}$

$$
\begin{aligned}
D_{1,n}(1,1) &= -\cos(\delta\hat{\phi}_n^- + \frac{T}{2}\delta\hat{\omega}_n^-) \\
D_{1,n}(2,2) &= -\frac{T^2}{4}\cos(\delta\hat{\phi}_n^- + \frac{T}{2}\delta\hat{\omega}_n^-) \\
D_{1,n}(1,2) &= D_{1,n}(2,1) = -\frac{T}{2}\cos(\delta\hat{\phi}_n^- + \frac{T}{2}\delta\hat{\omega}_n^-) \\
D_{1,n}(1,3) &= D_{1,n}(2,3) = D_{1,n}(3,1) = D_{1,n}(3,2) = D_{1,n}(3,3) = 0
\end{aligned}
\tag{4.38}
$$

$$
\begin{aligned}
D_{2,n}(1,1) &= -\sin(\delta\hat{\phi}_n^- + \frac{T}{2}\delta\hat{\omega}_n^-) \\
D_{2,n}(2,2) &= -\frac{T^2}{4}\sin(\delta\hat{\phi}_n^- + \frac{T}{2}\delta\hat{\omega}_n^-) \\
D_{2,n}(1,2) &= D_{2,n}(2,1) = -\frac{T}{2}\sin(\delta\hat{\phi}_n^- + \frac{T}{2}\delta\hat{\omega}_n^-) \\
D_{2,n}(1,3) &= D_{2,n}(2,3) = D_{2,n}(3,1) = D_{2,n}(3,2) = D_{2,n}(3,3) = 0
\end{aligned}
\tag{4.39}
$$

The time-predict equations are left intact as in (4.9) and (4.10), as our system description itself is linear, thus no need for higher order Taylor expansions. However, the measurement update equations, as provided by [12], will be:

$$\Lambda_n(i,j) = \frac{1}{2} \cdot \text{Tr}(D_{i,n} P_n^- D_{j,n} P_n^-) \tag{4.40}$$

$$K_n = P_n^- H_n^T (H_n P_n^- H_n^T + R_{\vartheta\vartheta} + \Lambda_n)^{-1} \tag{4.41}$$

$$\Pi_n = \frac{1}{2} K_n \sum_{i=1}^{m} \epsilon_i \text{Tr}(D_{i,n} P_n^-) \tag{4.42}$$

$$\hat{\mathbf{x}}_n = \hat{\mathbf{x}}_n^- + K_n(\mathbf{z}_n - h(\hat{\mathbf{x}}_n^-, 0)) - \Pi_n \tag{4.43}$$

$$P_n = (I - K_n H_n) P_n^- \tag{4.44}$$

$$\mathbf{u}_n = -K_x \hat{\mathbf{x}}_n \tag{4.45}$$

where

Λ_n: is the gain correction matrix.

Π_n: is the correction vector for posteriori state estimate.

Similarly to the enhanced first order filter, this model is even more complex due to the need to evaluate the Hessian matrices. Just like the enhanced first order filter it is expected to have an excellent performance with an extra boost due the reduced linearization error.

4.4.1 Comparison of First and Second order EKF

For the measurements model I&Q-a, which does not take into consideration the acceleration effect in the correlation, a second order EKF shows exactly the same performance as the first order EFK. Furthermore, we considered the correcting vector Π as a metric to measure the contribution of the second term in the Taylor expansion of the mapping function. Accordingly, $\Pi = \mathbf{0}$ for I&Q-a. This result suggests that the model is close to linear and that the linearzation errors occurring are minimal or at least they do not exist in the second derivatives of the mapping function $G^{(1)}(\cdot)$.

On the other hand, when I&Q-b is considered along with its mapping function $G^{(2)}(\cdot)$ and the Fresnel integrals it contains, the second order filter proved that it can further improve the performance by reducing the linearization error of the more sophisticated mapping function $G^{(2)}(\cdot)$. The effect was studied under the same deterministic high dynamics scenario introduced in section 4.3.2 shown once more in figure 4.7. Figure 4.8 shows that the bias θ_e caused by the dynamics is further reduced while the jitter is the same. As expected EKF does not improve the performance of I&Q-a. The Π metric is provided for this scenario in figure 4.9 and

47
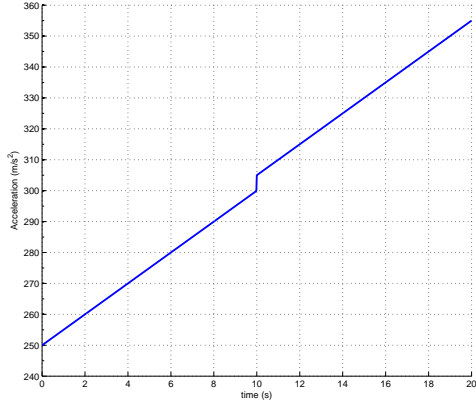
Figure 4.7: Acceleration scenario
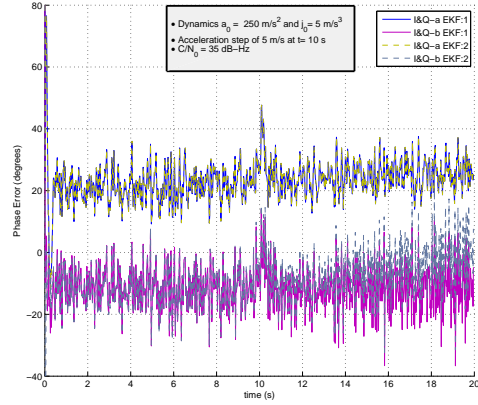
Figure 4.8: Phase Error of the first and second order EKF. Note that the second order EKF show improvement only for I&Q-b
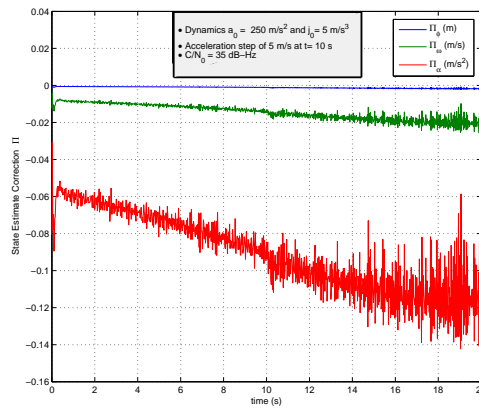
Figure 4.9: The state linearization correction vector Π for the second order EKF with the I&Q-b EKF:2 measurement model

shows the amount of correction added to the states over time. It is obvious that with increasing acceleration values the correction becomes higher. Furthermore, this effect seems to be linearly related to the acceleration.

The same two acceleration random walk profiles used previously, were consid-
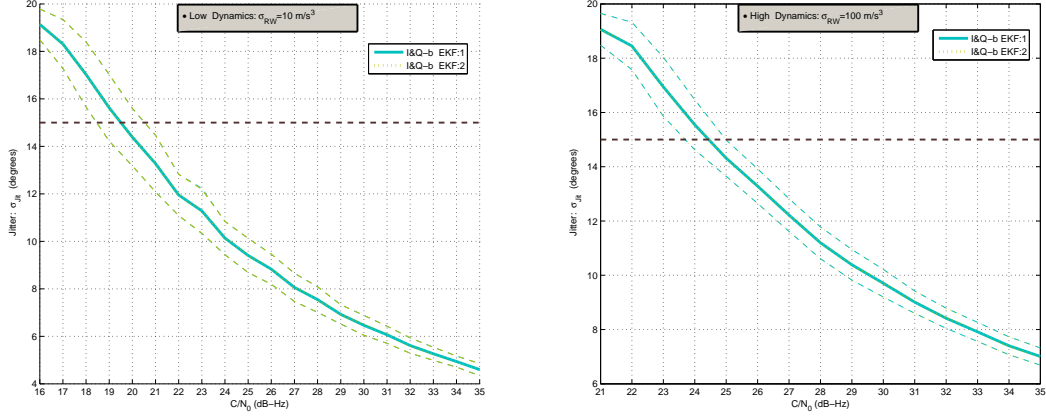
Figure 4.10: Phase jitter vs. C/N_0 for the first and second order EKF with the low (left) and high (right) dynamics profiles

ered for the purpose of comparing the first and second order EKF implementations in regards to the phase jitter. The results presented by figure 4.10 show the same jitter performance for both systems regardless the intensity of the dynamics. Again, this is due to the same reason stated above. Namely, the second order correction of the states comes as a shift whose value is directly related to the acceleration.

4.5   NCO Order and The Control Law

.

For all measurement models shown in section 4.3.1 all the states of the system are observable. The observability matrix given by

$$\zeta_O = \begin{bmatrix} H \\ H\Phi \\ H\Phi^2 \end{bmatrix} \tag{4.46}$$

can be easily checked to be full rank for the first two measurement models of 4.3.1.1 and 4.3.1.2. Additionally, although the derivation of the observability matrix, is not strait forward for the dual I_n and Q_n measurement model, one can argue that the states are definitely observable as they were shown to be observable with less accurate observation models.

In the following the control law for several NCO orders will be shown.

49

4.5.1 Second Order NCO

In a second order NCO one can control the frequency of the generated replica signal, keeping in mind that the phase is maintained continuous between epoch transitions. Therefore, the control input and the control driving matrix are chosen to be

$$(4.47)$$

$$\mathbf{u}_n = \omega_{NCO,n} - \omega_{NCO,n-1} \qquad \text{and} \qquad \Gamma = \begin{bmatrix} 0 \\ -1 \\ 0 \end{bmatrix} \qquad (4.48)$$

With a second order NCO the system is not fully controllable. In fact only the first two states are only controllable. This can be seen in (4.56) as the controllably matrix ζ_C is rank deficient.

$$\zeta_C = \begin{bmatrix} \Gamma & \Phi\Gamma & \Phi^2\Gamma \end{bmatrix} = - \begin{bmatrix} 0 & T & 2T \\ 1 & 1 & 1 \\ 0 & 0 & 0 \end{bmatrix} \qquad (4.49)$$

For this reason a partial controllability on a reduced system model scheme is derived with reduced states $\mathbf{x} = [\delta\phi \quad \delta\omega]^T$ as follows

$$\begin{aligned} \mathbf{x}_n &= \Phi'\mathbf{x}_{n-1} + \Gamma'\mathbf{u}_n \\ &= \begin{bmatrix} 1 & T \\ 0 & 1 \end{bmatrix} \mathbf{x}_{n-1} + \begin{bmatrix} 0 \\ -1 \end{bmatrix} (\omega_{NCO,n} - \omega_{NCO,n-1}) \end{aligned} \qquad (4.50)$$

The design of a control law lies in the choice of the control gain matrix K_x where $\mathbf{u} = -K_x\mathbf{x}$.

As devised in [13] the hypothetical regulator system has the following characteristic equation

$$\left| zI - \begin{bmatrix} 1 & T \\ 0 & 1 \end{bmatrix} + \begin{bmatrix} 0 \\ -1 \end{bmatrix} K_x \right| = 0$$

$$\text{or} \quad z^2 - (k_2 + 2)z - Tk_1 + k_2 + 1 = 0 \qquad (4.51)$$

Two poles z_1 and z_2 must be appropriately chosen before we solve for K_x. For stability the poles should lie inside the unit circle more over their value will affect the characteristics of the system in terms of settle time and maximum overshoot. An excellent choice is $z_1 = z_2 = 0$ which was validated experimentally to guarantee fast lock (around $5\,T$ samples).

Although the configuration of a double pole at zero showed good performance. The pole placement could be also systematically designed in analogy with the linearized PLL model. That is by simply using the using the discreet time transfer function of the second order PLL which can be found in [14]:

$$H_{\text{PLL}} = \frac{4\xi\omega_n T + (\omega_n T)^2 + 2(\omega_n T)^2 z^{-1} + (\omega_n T)^2 - 4\xi\omega_n T)}{(4 + 4\xi\omega_n T + (\omega_n T)^2) + (2(\omega_n T)^2 - 8)z^{-1} + (4 + 4\xi\omega_n T + (\omega_n T)^2)z^{-2}}$$

(4.52)

where:

ξ is the damping ratio of the PLL.

$\omega_n = \frac{8\xi B_n}{4\xi^2+1}$ is the natural frequency of the PLL.

Finally equating the denominator of (4.52) with the characteristic equation given in (4.51) yields to the desired values of $K_x = [k_1 \quad k_2]$

Because the acceleration is not a controllable state of the system, acceleration will lead to a constant bias in the phase error. Nevertheless, this bias can be reduced by a smart way to update the control input using the extra information we know about the acceleration. In fact, acceleration could be understood as a disturbance on the reduced system. Thus the control input update equation becomes

$$\mathbf{u}_n = - \begin{bmatrix} k_1 & k_2 & k_d \end{bmatrix} \begin{bmatrix} \delta\hat{\phi}_n \\ \delta\hat{\omega}_n \\ \delta\hat{\alpha}_n \end{bmatrix}$$

(4.53)

Where the gain k_d is the disturbance gain. It can be shown, using [15], that for a system with a disturbance d and disturbance driving matrix $\Psi = \begin{bmatrix} \frac{T^2}{2} \\ T \end{bmatrix}$ such that:

$$\begin{aligned} \mathbf{x}_n &= \Phi'\mathbf{x}_{n-1} + \Gamma'\mathbf{u}_n + \Psi d \\ &= \begin{bmatrix} 1 & T \\ 0 & 1 \end{bmatrix} \mathbf{x}_{n-1} + \begin{bmatrix} 0 \\ -1 \end{bmatrix} (\omega_{NCO,n} - \omega_{NCO,n-1}) + \begin{bmatrix} \frac{T^2}{2} \\ T \end{bmatrix} \hat{\alpha}_n \end{aligned}$$

(4.54)

the gain k_d minimizing the disturbance can be found using:

$$\begin{aligned} K_d &= -(\Gamma^T\Gamma)^{-1}\Gamma^T\Psi \\ &= T \end{aligned}$$

(4.55)

however a better value of $K_d = 1.58 \times T$ was determined experimentally and guaranteed a phase error extremely close to zero for constant accelerations.

The results shown in section 4.6 which are related to EKF tracking based on a second order NCO are obtained using a double pole at zero, that is equivalent to $k_1 = \frac{1}{T}$ and $k_2 = 2$. Additionally, $k_d = 1.58T$ was adopted.

4.5.2 Third Order NCO

A third order NCO is simply an oscillator that generates a sinusoidal signal at a specified frequency change rate. Moreover, The phase and frequency of the output signal, are maintained continuous.

For a third order NCO the first three states are controllable and therefore the system described in (4.1) is fully controllable. That can be seen by verifying that the controllability matrix is full rank, where the controllability matrix ζ_C is given by:

$$\zeta_C = \begin{bmatrix} \Gamma & \Phi\Gamma & \Phi^2\Gamma \end{bmatrix} = - \begin{bmatrix} 0 & \frac{T^2}{2} & 2T^2 \\ 0 & T & 2T \\ 1 & 1 & 1 \end{bmatrix} \tag{4.56}$$

The control law is $\mathbf{u}_n = -K_x \mathbf{x}_n$ with $\mathbf{x} = \begin{bmatrix} \delta\phi & \delta\omega & \delta\alpha \end{bmatrix}^T$ and K_x could be found solving the characteristic equation

$$\left| zI - \begin{bmatrix} 1 & T & \frac{T^2}{2} \\ 0 & 1 & T \\ 0 & 0 & 1 \end{bmatrix} + \begin{bmatrix} 0 \\ 0 \\ -1 \end{bmatrix} K_x \right| = 0 \tag{4.57}$$

With two of the three poles obtained from (4.52) and a third pole at zero. Nevertheless, the choice of the first two poles is more delicate here than it is in the case for a second order NCO. A bandwidth value B_n not smaller than 10 Hz guarantees stability and lock for scenarios of high dynamics. It is important to note here that the value chosen for B_n does not directly affect the noise behavior in contrast to a PLL where it used to explicitly decide the bandwidth of the loop filter. Although for the EKF the choice of $Q_{\nu\nu}$ and $R_{\vartheta\vartheta}$ determine the noise behavior, B_n still has an implicit effect and therefore we will consider the same value of B_n in order to build an equal ground of comparison among our systems.

4.5.3 Fourth Order NCO

A fourth order NCO is an oscillator that generates a sinusoidal signal according to a depicted change rate of "frequency change rate", which is in other words a jerk equivalent term.

In order to achieve this implementation the process model was augmented with one additional state, namely jerk. The augmented system is highly similar to the third order NCO system, and therefore the details will be omitted here. It should be noted however that the fourth pole was chosen at zero.
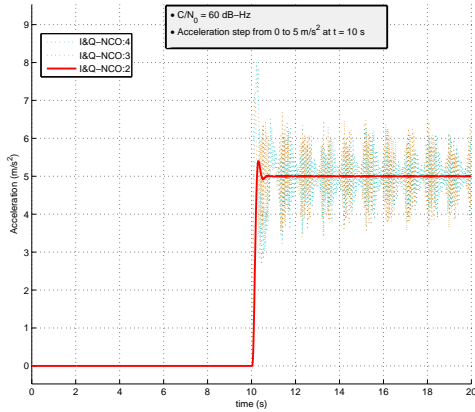
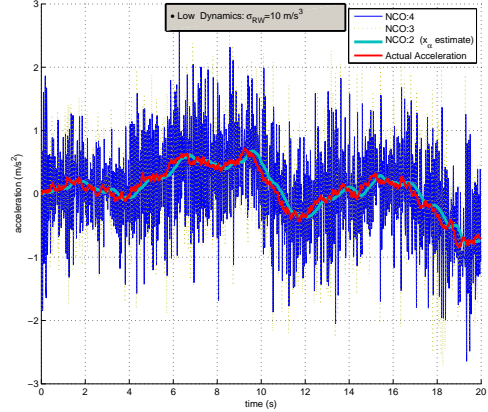Figure 4.11: Acceleration estimate with an acceleration step as input

Figure 4.12: Acceleration estimate with the low intensity acceleration random walk as input

Additionally, the process model in the previously described systems with lower NCO order were also augmented. The augmented versions of these systems will be used whenever a direct comparison with the fourth order NCO is carried.

4.5.4 Comparison of NCOs with Different Order

In both figures 4.11 and 4.12 we observe that the acceleration component of the third and fourth order NCO is highly noisy. It can be concluded from figure 4.11 that this high variation start after a change in the dynamics and is not initiated by the random noise. This leaves us with the plausible conclusion that the control of the system becomes harder with higher NCO orders. Fortunately, this extra noise present in the acceleration estimate will drop out when estimating the phase as the process includes a double integration which is equivalent to low pass filtering this noise. Nevertheless, figure 4.13 shows that the phase jitter is higher for higher order NCO. Precisely, the system equipped with a third order NCO shows a slight degradation in jitter performance when compared to a system with second order NCO. In the low dynamics situation, the fourth order suffers severely from degradation where it even fails to lock in the high dynamics scenario. We conclude this analysis that the higher order NCO systems need to be carefully designed as they are more vulnerable to instabilities.
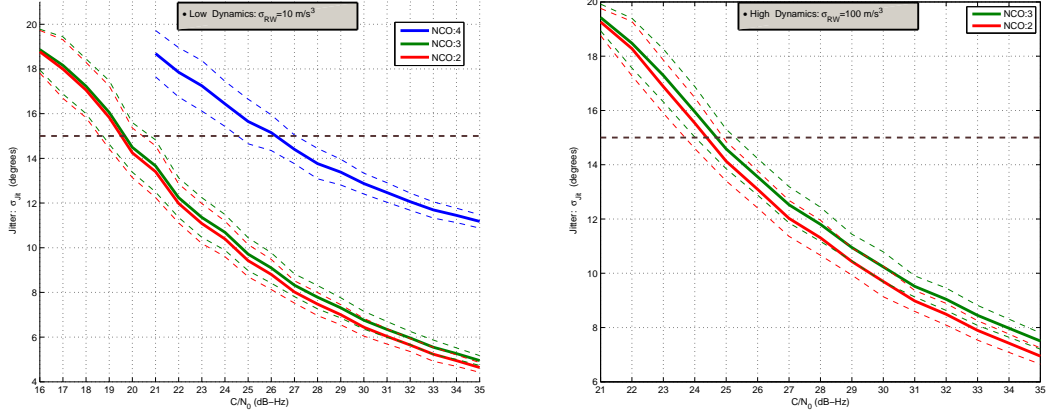
Figure 4.13: Phase jitter vs. C/N$_0$ for the second, third and fourth order NCO using the I&Q-b measurement model with the low (left) and high (right) dynamics profiles

4.6 Comparison of the EKF solution and the third order PLL with optimal PLL noise Bandwidth

In this section we import the phase jitter results of the PLL simulated with the optimal noise bandwidth B_n and compare it the the first order EKF using the I&Q-b measurement model. Again, the results refer to the two of low and high random walk acceleration profiles shown in 3.7.

The EKF has a complete knowledge about the process and the statistics of the disturbances involved. On the other hand, since the optimal PLL noise bandwidth was derived specifically for each of dynamics scenarios, the PLL is considered to have to a certain extent, awareness about the intensity of these dynamics. In other words, this setup is the most fair basis that can be made in order to compare the two systems.

The results in figure 4.14 show that the EKF solution has a better performance than the PLL for weak signals. Nevertheless, the traditional PLL outstands the EKF system for high C/N$_0$ signals. Moreover, the EKF provides a higher ability to cope with rapidly changing dynamics. This can be seen in the increase of the C/N$_0$ level that decides the better performing system. For instance, the EKF system outperforms the PLL for weak signals ranging until C/N$_0$ = 24 dB-Hz in the low dynamics scenario, while this C/N$_0$ separating level increases up to 34 dB-Hz in the case of the high dynamics scheme. This can be understood as the
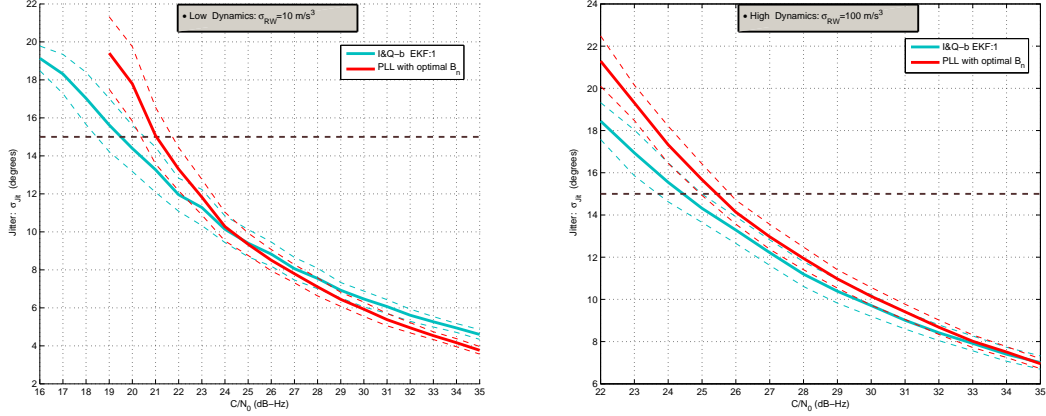
Figure 4.14: Phase jitter vs. C/N_0 for the third order PLL with optimal B_n and the EKF with I&Q-b measurement model and an EKF tracking system equiped with a second order NCO and I&Q-b measurement model. Comparisons are with the low (left) and high (right) dynamics profiles

EKF has a complete knowledge about the signal dynamics process while the PLL, although it has a customized noise bandwidth for the specific dynamic scenario, has a limited knowledge about the process. Therefore, with increasing dynamic disturbances the PLL estimation errors increase. Because the disturbance process is statistically described in the EKF, the phase estimation errors of the EKF also increase due to disturbance. Nevertheless, these estimation errors are much more severe in the PLL leading to a increasing shift in the C/N_0 separation level of performance.

This result shows that there is a benefit in the EKF solution. Additionally, both systems have a tuning parameter against dynamic stress. Namely B_n for the PLL and the intensity factor of the disturbance covariance matrix for the EKF. Nevertheless, it is easier to come up with a compromising B_n value for the PLL than it is the case choosing the intensity factor of the EKF.

Chapter 5

Conclusion

5.1   Summary

The effect of high dynamics on the GNSS receiver tracking performance was studied. The focus of this work was to exploit this effects in the code and signal correlation processes that take places in both code and carrier tracking loops.

Although dynamics affect the code loop, these effect can be neglected as they do not induce the loop to loosing code lock. Furthermore this effect was determined to be in the order of a tenth of a millimeter in realistic dynamic situations.

A Simulation model to study the effect of high dynamics on PLL tracking was developed based on the conventional linearized model. Analytical formulation of the signal correlation stage was needed to empower the model with a more accurate simulation of the of correlation procedure under high accelerations. It was shown that PLL jitter is affected by changing dynamic conditions while high constant accelerations values have negligible effect on the PLL performance. The optimal noise bandwidth for two different random walk dynamic scenarios was obtained. The results show that the optimal noise bandwidth is higher when the dynamic variations are more intense in order to compensate for dynamic stress. Additionally the results of the simulation were validated using an intermediate frequency implementation.

The derivation exploiting the effect of acceleration on signal correlation was used as an observation model in an EKF tracking system. The proposed system showed that it is able to cope with high dynamics by increasing the margin of maximum allowed dynamic stress, nevertheless the result was not clearly validated with randomly varying dynamics. Different measurement models were also presented and compared. The measurement models using both accumulated in-phase and quadrature measurement showed the best performances with respect to single measurement models.

The second order EKF implementation was also studied, and the EKF configured with the enhanced measurement model showed improvement and potential to benefit from reduction in the linearization errors.

Different control laws were investigated specifically by increasing the NCO order. Frequency controlled (second order) oscillators showed that they are the simplest and most robust to control the system and provided better stability and performance.

The EKF system was generally compared to the traditional PLL on "as fair as possible" comparison basis and the EKF shows benefits over PLL especially with increasing dynamic variations.

5.2   Future Work

For future work, the proposed EKF solution will be validated under several dynamic scenarios based on specific applications and dynamics profiles. Furthermore, a more precise derivation of the Hessian matrix of second order EKF should be carried and its effect on performance should be analyzed. Additionally, the implementation of a square root form of the filter is required to avoid potential numerical errors associated with the Kalman filter. Finally, a heuristic approach to update the EKF disturbance tuning factor based on the dynamic history and instantaneous acceleration tendencies is currently under study.

Appendix A

Fresnel Integrals

C(x) and S(x), shown in figure A.1, are two transcendental functions named after Augustin-Jean Fresnel, they are described by the following two integrals.

$$\text{C}(x) = \int_0^x \cos(t^2)\, dt \tag{A.1}$$

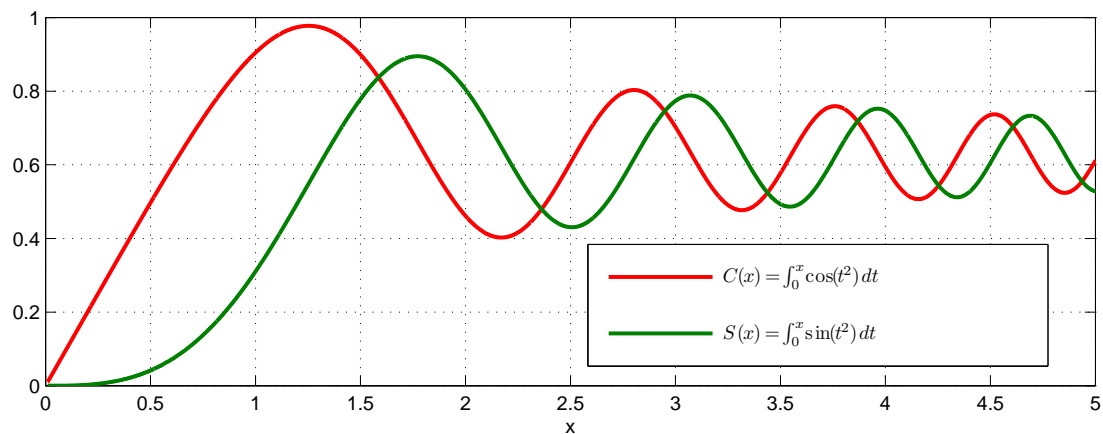$$\text{S}(x) = \int_0^x \sin(t^2)\, dt \tag{A.2}$$

Figure A.1: Plot of Fresnel integrals

A.1 Useful Relations

The power series expansion of these functions are

$$S(x) = \int_0^x \sin(t^2)\, dt = \sum_{n=0}^{\infty} (-1)^n \frac{x^{4n+3}}{(4n+3)(2n+1)!} \tag{A.3}$$

$$C(x) = \int_0^x \cos(t^2)\, dt = \sum_{n=0}^{\infty} (-1)^n \frac{x^{4n+1}}{(4n+1)(2n)!} \tag{A.4}$$

Their relation to the error funtion erf, presented in [16] is

$$S(x) = \frac{\sqrt{\pi}}{4} \left(\sqrt{i}\ \mathrm{erf}\,^1\sqrt{i}\,x) + \sqrt{-i}\ \mathrm{erf}(\sqrt{-i}\,x) \right) \tag{A.5}$$

$$C(x) = \frac{\sqrt{\pi}}{4} \left(\sqrt{-i}\ \mathrm{erf}(\sqrt{i}\,x) + \sqrt{i}\ \mathrm{erf}(\sqrt{-i}\,x) \right) \tag{A.6}$$

The symmetry relations are as follows

$$C(-x) = -C(x) \tag{A.7}$$
$$S(-x) = S(x) \tag{A.8}$$

A useful indefinite integral provided by [17] property is the following

$$\int \cos(ax^2 + 2bx + c)\, dx = \sqrt{\frac{\pi}{2a}} \left\{ \cos\frac{ac-b^2}{a} C\left(\frac{ax+b}{\sqrt{a}}\right) - \sin\frac{ac-b^2}{a} S\left(\frac{ax+b}{\sqrt{a}}\right) \right\} \tag{A.9}$$

$$\int \sin(ax^2 + 2bx + c)\, dx = \sqrt{\frac{\pi}{2a}} \left\{ \cos\frac{ac-b^2}{a} S\left(\frac{ax+b}{\sqrt{a}}\right) + \sin\frac{ac-b^2}{a} C\left(\frac{ax+b}{\sqrt{a}}\right) \right\} \tag{A.10}$$

with $a > 0$

A.2 Approximation

An approximation for the integral provided by [18] was used for the purpose of software implementation.

$$C'(x) = \int_0^x \cos(\frac{\pi}{2}t^2)\, dt \tag{A.11}$$

[1]The error function, also known as Gauss error function given by $\mathrm{erf}(x) = \frac{2}{\sqrt{\pi}} \int_0^x e^{-t^2} dt$

$$S'(x) = \int_0^x \sin(\frac{\pi}{2}t^2)\,dt \qquad (A.12)$$

The integrals are evaluated by a power series for $x < 1$. For $x \geq 1$ auxiliary functions $f(x)$ and $g(x)$ are employed such that

$$C'(x) = \frac{1}{2} + f(x)\sin(\frac{\pi}{2}x^2) - g(x)\cos(\frac{\pi}{2}x^2) \qquad (A.13)$$

$$S'(x) = \frac{1}{2} - f(x)\cos(\frac{\pi}{2}x^2) - g(x)\sin(\frac{\pi}{2}x^2) \qquad (A.14)$$

where the asymptotic power series expansion is used to approximate $f(x)$ and $g(x)$.

It is worth mentioning that for computational feasibility only the first 7 terms are considered for $x < 1$. For $x \geq 1$, we should consider 11 terms to reach the same accuracy. Moreover, simple addition of the terms would cause an arithmetic overflow, therefore a common denominator form need to be evaluated resulting in a polynomial which can be evaluated avoiding the overflow.

Next, in order to evaluate $C(x)$ and $S(x)$ the following property is used

$$C(x) = \sqrt{\frac{\pi}{2}} \times C'(\frac{2}{\pi}x) \qquad (A.15)$$

$$S(x) = \sqrt{\frac{\pi}{2}} \times S'(\frac{2}{\pi}x) \qquad (A.16)$$

The accuracy of the approximation is show in table A.1

Arithmetic	function	domain	# trials	peak	rms
IEEE	S(x)	0, 10	10000	2.0e-15	3.2e-16
IEEE	C(x)	0, 10	10000	1.8e-15	3.3e-16

Table A.1: Accuracy of the approximation: relative error

Appendix B

Noise Statistics After Correlation

The received signal and its statistics are:

$$S_i = A\cos(\omega_c t_i + \phi) + \eta_i \tag{B.1}$$

$$\eta_i = \eta_{I,i}\cos\omega_c t_i + \eta_{Q,i}\sin\omega_c t_i \tag{B.2}$$

$$E\{\eta_{I,i}\} = E\{\eta_{Q,i}\} = E\{\eta_{I,i}.\eta_{Q,j}\} = 0 \tag{B.3}$$

$$E\{\eta_{I,i}.\eta_{I,j}\} = E\{\eta_{Q,i}.\eta_{Q,j}\} = \delta(i-j)\sigma_s \tag{B.4}$$

After correlation we get:

$$I = \frac{2}{N}\sum_{i=0}^{N} S_i \cos(\omega_c t_i + \hat{\phi}) \tag{B.5}$$

$$E\{I\} = \frac{2}{N}\sum_{i=0}^{N} E\{S_i\}\cos(\omega_c t_i + \hat{\phi})$$

$$= \frac{2}{N}\sum_{i=0}^{N} A\cos(\omega_c t_i + \phi)\cos(\omega_c t_i + \hat{\phi}) \tag{B.6}$$

$$= \frac{2}{N}\sum_{i=0}^{N} \frac{A}{2}\cos(\phi - \hat{\phi})$$

$$= A\cos(\phi - \hat{\phi})$$

$$\mathrm{Var}(I) = E\{I^2\} - E\{I\}^2 \tag{B.7}$$

$$
E\{I^2\} = E\left\{ \frac{2}{N} \sum_{i=0}^{N} \left[A\cos(\omega_c t_i + \phi) + \eta_{I,n}\cos(\omega_c t_i) + \eta_{Q,i}\sin(\omega_c t_i) \right].\cos(\omega_c t_i + \hat{\phi}) \right.
$$

$$
\left. .\frac{2}{N} \sum_{j=0}^{N} \left[A\cos(\omega_c t_j + \phi) + \eta_{I,j}\cos(\omega_c t_j) + \eta_{Q,n}\sin(\omega_c t_j) \right].\cos(\omega_c t_j + \hat{\phi}) \right\}
$$

$$
= \frac{4}{N^2} \sum_{i=0}^{N}\sum_{j=0}^{N} \left\{ \left[A\cos(\omega_c t_i + \phi)\cos(\omega_c t_i + \hat{\phi}) \right.\right.
$$

$$
\left. +\eta_{I,i}\cos(\omega_c t_i)\cos(\omega_c t_i + \hat{\phi}) + \eta_{Q,i}\sin(\omega_c t_i)\cos(\omega_c t_i + \hat{\phi}) \right]
$$

$$
. \left[A\cos(\omega_c t_j + \phi)\cos(\omega_c t_j + \hat{\phi}) \right.
$$

$$
\left.\left. +\eta_{I,j}\cos(\omega_c t_j)\cos(\omega_c t_j + \hat{\phi}) + \eta_{Q,j}\sin(\omega_c t_j)\cos(\omega_c t_j + \hat{\phi}) \right] \right\}
$$

$$
= \frac{4}{N^2} \left(\sum_{i=0}^{N} A\cos(\omega_c t_i + \phi)\cos(\omega_c t_i + \hat{\phi}) \right).\left(\sum_{j=0}^{N} A\cos(\omega_c t_j + \phi)\cos(\omega_c t_j + \hat{\phi}) \right)
$$

$$
+ \frac{4}{N^2} \sum_{i=0}^{N} \sigma_s^2\cos^2(\omega_c t_i)\cos^2(\omega_c t_i + \hat{\phi}) + \frac{4}{N^2} \sum_{i=0}^{N} \sigma_s^2\sin^2(\omega_c t_i)\cos^2(\omega_c t_i + \hat{\phi})
$$

$$
= \frac{4}{N^2} \left[\frac{N^2 A^2}{4}\cos^2(\phi - \hat{\phi}) + \sum_{i=0}^{N} \sigma_s^2\frac{1}{4}\left(\cos(-\hat{\phi}) + \cos(2\omega_c t_i + \hat{\phi}) \right)^2 \right.
$$

$$
\left. + \sum_{i=0}^{N} \sigma_s^2\frac{1}{4}\left(\sin(-\hat{\phi}) + \sin(2\omega_c t_i + \hat{\phi}) \right)^2 \right]
$$

$$
= A^2\cos^2(\phi - \hat{\phi})
$$

$$
+ \frac{1}{N^2}\sigma_s^2 \sum_{i=0}^{N} \left(\cos^2(-\hat{\phi}) + \cos^2(2\omega_c t_i + \hat{\phi}) + 2\cos(-\hat{\phi})\cos(2\omega_c t_i + \hat{\phi}) \right.
$$

$$
\left. + \sin^2(-\hat{\phi}) + \sin^2(2\omega_c t_i + \hat{\phi}) + 2\sin(-\hat{\phi})\sin(2\omega_c t_i + \hat{\phi}) \right)
$$

$$
= A^2\cos^2(\phi - \hat{\phi}) + \frac{1}{N^2}\sigma_s^2 \sum_{i=0}^{N} 2 + 2\underbrace{\cos(2\omega_c t_i + 2\hat{\phi})}_{\text{double freq}}
$$

$$
= A^2\cos^2(\phi - \hat{\phi}) + \frac{2}{N}\sigma_s^2 \tag{B.8}
$$

$$
\Rightarrow \boxed{\mathrm{Var}(I) = \frac{2}{N}\sigma_s^2} \tag{B.9}
$$

Appendix C

Covariance Matrix of Process Disturbance

Assuming we have N states describing our system, the covariance matrix $Q_{\nu\nu}$ of the process disturbance ν becomes a $N \times N$ matrix and can be obtained as follows

$$Q_{\nu\nu} = E \left\{ \begin{bmatrix} \nu_1 \\ \nu_2 \\ \vdots \\ \nu_N \end{bmatrix} . \begin{bmatrix} \nu_1 & \nu_2 & \cdots & \nu_N \end{bmatrix} \right\} \tag{C.1}$$

We recall that

$$\nu_k = \int_{(n-1)T}^{nT} \frac{(nT - \tau)^{N-k}}{(N-k)!} Y(\tau) \, d\tau, \qquad k = 1, 2, 3, ..., N \text{ standing for } \omega, \alpha \text{ and } j \, ... \tag{C.2}$$

Therefore

$$Q_{\nu\nu}(k, l) = E \left\{ \int_{(n-1)T}^{nT} \frac{(nT - \tau)^{N-k}}{(N-k)!} Y(\tau) \, d\tau . \int_{(n-1)T}^{nT} \frac{(nT - \rho)^{N-l}}{(N-l)!} Y(\rho) \, d\rho \right\} \tag{C.3}$$

$$= \int_{(n-1)T}^{nT} \int_{(n-1)T}^{nT} \frac{\tau^{N-l}}{(N-l)!} \frac{\rho^{N-k}}{(N-k)!} . E\left\{ Y(\tau).Y(\rho) \right\} \, d\tau \, d\rho \tag{C.4}$$

But since $Y(t)$ is white random noise of dynamics order $N + 1$, for example it would be a white jerk stress noise if N is 3, we have

$$E\left\{ Y(\tau).Y(\rho) \right\} = \sigma_N^2 . T^2 . \delta(\tau - \rho) \tag{C.5}$$

Replacing above and using the integration property of the dirac delta we get

$$Q_{\nu\nu}(k,l) = \sigma_j^2 . T^2 \int_{(n-1)T}^{nT} \frac{(nT - \tau)^{N-k}.(nT - \tau)^{N-l}}{(N - k)! \times (N - l)!} \, d\tau \qquad (\text{C.6})$$

$$= \sigma_j^2 \frac{T^{2N-k-l+3}}{(2N - l - k + 1) \times (N - l)! \times (N - k)!} \qquad (\text{C.7})$$

Appendix D

Jacobian Matrix with Acceleration

$$H_n = \begin{bmatrix} h_{11} & h_{12} & h_{13} \\ h_{21} & h_{22} & h_{23} \end{bmatrix} \tag{D.1}$$

We define the following terms:

$$A = \delta\tilde{\phi}_n - \frac{\delta\hat{\omega}_n^2}{4\alpha_{0,n}} \tag{D.2}$$

$$B_1 = \frac{\frac{\delta\hat{\omega}_n}{2}}{\sqrt{\alpha_{0,n}}} \tag{D.3}$$

$$B_2 = \frac{\alpha_{0,n}T + \frac{\delta\hat{\omega}_n}{2}}{\sqrt{\alpha_{0,n}}} \tag{D.4}$$

$$D_1 = \frac{\omega_n}{4\alpha\sqrt{\alpha}} \tag{D.5}$$

$$D_2 = \frac{\alpha T + \frac{\omega_n}{2}}{2\alpha\sqrt{\alpha}} \tag{D.6}$$

$$\tag{D.7}$$

The elements of H_n take the form:

$$h_{11} = \frac{1}{T\sqrt{\alpha}}\left(\sin\left(A\right)\left(\mathrm{C}\left(B_2\right) - \mathrm{C}\left(B_1\right)\right) + \cos\left(A\right)\left(\mathrm{S}\left(B_2\right) - \mathrm{S}\left(B_1\right)\right)\right) \tag{D.8}$$

$$h_{21} = \frac{-1}{T\sqrt{\alpha}}\left(\sin\left(A\right)\left(\mathrm{S}\left(B_2\right) - \mathrm{S}\left(B_1\right)\right) - \cos\left(A\right)\left(\mathrm{C}\left(B_2\right) - \mathrm{C}\left(B_1\right)\right)\right) \tag{D.9}$$

$$h_{12} = \frac{1}{T\sqrt{\alpha}}\left(\frac{\omega}{2\alpha}\sin(A)\big(\mathrm{C}(B_2) - \mathrm{C}(B_2)\big) - \frac{1}{2\sqrt{\alpha}}\cos(A)\big(\cos(B_2^2) - \cos(B_1^2)\big)\right.$$
$$\left. + \frac{\omega}{2\alpha}\cos(A)\big(\mathrm{S}(B_2) - \mathrm{S}(B_2)\big) + \frac{1}{2\sqrt{\alpha}}\sin(A)\big(\sin(B_2^2) - \sin(B_1^2)\big)\right)$$
$$\text{(D.10)}$$

$$h_{22} = \frac{-1}{T\sqrt{\alpha}}\left(\frac{\omega}{2\alpha}\sin(A)\big(\mathrm{S}(B_2) - \mathrm{S}(B_2)\big) - \frac{1}{2\sqrt{\alpha}}\cos(A)\big(\sin(B_2^2) - \sin(B_1^2)\big)\right.$$
$$\left. - \frac{\omega}{2\alpha}\cos(A)\big(\mathrm{C}(B_2) - \mathrm{C}(B_2)\big) - \frac{1}{2\sqrt{\alpha}}\sin(A)\big(\cos(B_2^2) - \cos(B_1^2)\big)\right)$$
$$\text{(D.11)}$$

$$h_{13} = \frac{-1}{2T\alpha\sqrt{\alpha}}\left(\cos(A)\big(\mathrm{C}(B_2) - \mathrm{C}(B_1)\big) - \sin(A)\big(\mathrm{S}(B_2) - \mathrm{S}(B_1)\big)\right)$$
$$+ \frac{1}{T\sqrt{\alpha}}\left((\frac{\omega}{2\alpha})^2\sin(A)\big(\mathrm{C}(B_2) - \mathrm{C}(B_1)\big) + \cos(A)(D_2\cos(B_2^2) - D_1\cos(B_1^2))\right.$$
$$\left. + (\frac{\omega}{2\alpha})^2\cos(A)\big(\mathrm{S}(B_2) - \mathrm{S}(B_1)\big) - \sin(A)\big(D_2\sin(B_2^2) - D_1\sin(B_1^2)\big)\right)$$
$$\text{(D.12)}$$

$$h_{23} = \frac{1}{2T\alpha\sqrt{\alpha}}\left(\cos(A)\big(\mathrm{S}(B_2) - \mathrm{S}(B_1)\big) + \sin(A)\big(\mathrm{C}(B_2) - \mathrm{C}(B_1)\big)\right)$$
$$+ \frac{1}{T\sqrt{\alpha}}\left(-(\frac{\omega}{2\alpha})^2\sin(A)\big(\mathrm{S}(B_2) - \mathrm{S}(B_1)\big) + \cos(A)\big(D_2\sin(B_2^2) - D_1\sin(B_1^2)\big)\right.$$
$$\left. + (\frac{\omega}{2\alpha})^2\cos(A)\big(\mathrm{C}(B_2) - \mathrm{C}(B_1)\big) + \sin(A)(D_2\cos(B_2^2) - D_1\cos(B_1^2))\right)$$
$$\text{(D.13)}$$

Bibliography

[1] C. Günther, *Satellite Navigation Lecture Notes. Lecture notes.* München: Technische Universitt München, 2008.

[2] B. Parkinson, *Global Positioning System: Theory and Applications.* Washington: AIAA (American Institute of Aeronautics and Astronautics), 1996.

[3] E. D. Kaplan, *Understanding GPS-Principles and Applications.* Boston: Artech House Publisher, 2006.

[4] D.-J. Jwo, "Optimisation and sensitivity analysis of GPS receiver tracking loops in dynamic environments," *Radar, Sonar and Navigation, IEE Proceedings -*, vol. 148, pp. 241–250, Aug 2001.

[5] F. Castella, "An adaptive two-dimensional kalman tracking filter," *Aerospace and Electronic Systems, IEEE Transactions on*, vol. AES-16, pp. 822–829, Nov. 1980.

[6] V. Vilnrotter, S. Hinedi, and R. Kumar, "Frequency estimation techniques for high dynamic trajectories," *Aerospace and Electronic Systems, IEEE Transactions on*, vol. 25, pp. 559–577, Jul 1989.

[7] D. Simon and H. El-Sherief, "Hybrid kalman/minimax filtering in phase-locked loops," *American Control Conference, 13th, Baltimore, MD. UNITED STATES*, pp. 2212–2216, June 29 1994.

[8] M. L. Psiaki, "Smoother-based GPS signal tracking in a software receiver," Nov. 01 2000.

[9] M. L. Psiaki and H. Jung, "Extended kalman filter methods for tracking weak GPS signals," *15th International Technical Meeting of the Satellite Division of The Institute of Navigation ION GPS 2002*, vol. 53, pp. 20–31, Sept. 24 2002.

[10] C. ODriscoll and G. Lachapelle, "Comparison of traditional and kalman filter based tracking architectures," *European Navigation Conference 2009 (ENC09),Naples Italy*, vol. 53, pp. 40–51, May 3 2009.

[11] N. I. Ziedan and J. L. Garrison, "Extended kalman filter-based tracking of weak GPS signals under high dynamic conditions," *17th International Technical Meeting of the Satellite Division of the Institute of Navigation ION GNSS*, vol. 53, pp. 20–31, Sept. 19 2004.

[12] D. Simon, *Optimal State Estimation: Kalman, H Infinity, and Nonlinear Approaches.* New York: John Wiley & Sons, Inc, 2006.

[13] G. F. Franklin, D. J. Powell, and M. L. Workman, *Digital Control of Dynamic Systems (3rd Edition).* Prentice Hall, December 1997.

[14] K. Borre, *A Software-Defined GPS and Galileo Receiver : A Single-Frequency Approach.* Boston, EUA : Birkhäuser, 2007.

[15] J. Lunze, *Regelungstechnik 2: Mehrgrensysteme, Digitale Regelung.* Berlin: Springer, 2008.

[16] E. Milton, *Handbook of Mathematical Functions.* New York: Dover Publications, 1973.

[17] I. Gradshtein, *Table of Integrals, Series, and Products.* Boston: Academic Press, 2000.

[18] S. L. Moshier, "Cephes math library release 2.8," 2000.